7-3-2012

Coolant distribution control in satellite structural panels using electrohydrodynamic conduction pumping

Samuel Sinnamon

Samuel Sinnamon
Candidate

Mechanical Engineering
Department

This thesis is approved, and it is acceptable in quality and form for publication:

Approved by the Thesis Committee:

C Randall Truman , Chairperson

Arsalan Razani

Andrew Williams

COOLANT DISTRIBUTION CONTROL IN SATELLITE STRUCTURAL PANELS USING ELECTROHYDRODYNAMIC CONDUCTION PUMPING

by

SAMUEL SINNAMON

BACHELOR OF SCIENCE, MECHANICAL ENGINEERING
LAWRENCE TECHNOLOGICAL UNIVERSITY, 2009

THESIS

Submitted in Partial Fulfillment of the
Requirements for the Degree of

Masters of Science
Mechanical Engineering

The University of New Mexico
Albuquerque, New Mexico

May, 2012

ACKNOWLEDGEMENTS

I am thankful to my parents, who have always been an inspiration to me. I would also like to thank my faculty advisor, Randall Truman, for his valuable inputs, and my colleagues at the Air Force Research Laboratory Andrew Williams, Greg Busch, Brent Taft, Derek Hengeveld, and Joy Stein for their help every step of the way. This project was funded by the Air Force Office of Scientific Research, the Air Force Research Laboratory/Space Vehicles Directorate, and the New Mexico Space Grant Consortium, and accomplished in collaboration with the Mechanical, Materials, and Aerospace Engineering Department at the Illinois Institute of Technology and with NASA Goddard Space Flight Center.

COOLANT DISTRIBUTION CONTROL IN SATELLITE STRUCTURAL PANELS USING ELECTROHYDRODYNAMIC CONDUCTION PUMPING

by

SAMUEL SINNAMON

BACHELOR OF SCIENCE, MECHANICAL ENGINEERING,

LAWRENCE TECHNOLOGICAL UNIVERSITY, 2009

MASTERS OF SCIENCE, MECHANICAL ENGINEERING

ABSTRACT

Electrohydrodynamic (EHD) conduction pumping is well suited for pumping coolants in space-borne thermal control systems. Advantages of EHD pumps include light-weight, simple designs, no moving parts, fast response times, and low power consumption. The EHD conduction pumping phenomenon is a result of electrical conduction in highly resistive liquids, in which charge carriers are ions created by a reversible dissociation-recombination reaction. EHD pumps show promise as a means to actively control the distribution of coolants within a flow network and may be applied to

a novel biologically-inspired thermal control system. This experiment characterizes the performance of an EHD pump operating under various flow conditions and demonstrates the successful control of flow distribution between two parallel lines using the EHD pump in two configurations. The first configuration orients the EHD pump so that the net pumping forces act in the same direction as the flow velocity. In this case, the EHD pump pulls additional flow through the desired line. The second configuration orients the EHD pump such that the net pumping forces act in the direction opposite to the flow velocity. In this case, the EHD pump opposes the flow in its line, thereby forcing additional flow through the desired line, as one would use a valve. Results show that the latter configuration is more effective at controlling flow distribution between the two lines at total mass flow rates ranging from 0 to 7.7 g/s.

Table of Contents

List of Figures

List of Tables

Nomenclature

A	Surface area
A_w	Wetted area of the isogrid panel
b_i	Mobility of a charge of ith species
B	Total bias limit of a parameter
B_{dP}	Bias limit of total differential pressure across EHD pump
B_{dP_f}	Bias limit of differential pressure across EHD pump due to friction
$B_{dP_{net}}$	Bias limit of differential pressure across EHD pump due to EHD effects
$B_{I_{intek}}$	Bias limit of current output of mass flow meter
$B_{I_{RTD}}$	Bias limit of current through RTD
B_Q	Bias limit of volume flow rate through EHD pump
$B_{Q_{total\,mL}}$	Bias limit of total volume flow rate
$B_{Q_{2mL}}$	Bias limit of volume flow rate in line (2)
$B_{Q_{3g}}$	Total bias limit of mass flow rate in line (3)
$B_{Q_{3g}1}$	Bias limit of mass flow rate due to bias limit of voltage reading for the mass flow meter, $B_{V_{intek}}$
$B_{Q_{3g}2}$	Standard error estimate of curve-fit for mass flow meter calibration
$B_{Q_{3mL}}$	Bias limit of volume flow rate in line (3)
B_r	Bias limit of a result

B_{Re}	Bias limit of Reynolds number through EHD pump
$B_{R_{intek}}$	Bias limit of the resistor used in measuring mass flow rate in line (3)
$B_{R_{ref}}$	Bias limit of reference resistance used in measuring fluid temperature
$B_{R_{RTD}}$	Bias limit of RTD resistance
B_T	Total bias limit of fluid temperature
B_{T1}	Bias limit of fluid temperature due to the bias limit of the resistance of the RTD, $B_{R_{RTD}}$
B_{T2}	Bias limit of the RTD due to manufacturer calibration
B_v	Bias limit of flow velocity through EHD pump
B_V	Bias limit for a voltage measurement (data acquisition bias)
$B_{V_{intek}}$	Total bias limit of voltage reading for the mass flow meter
$B_{V_{intek}1}$	Bias limit of voltage reading for the mass flow meter due to the bias limit of current output, $B_{I_{intek}}$
$B_{V_{intek}2}$	Bias limit of voltage reading for the mass flow meter due to data acquisition unit
$B_{V_{ref}}$	Bias limit of RTD reference voltage due to data acquisition unit
$B_{V_{RTD}}$	Bias limit of voltage drop across RTD due to data acquisition unit
B_μ	Bias limit of the fluid dynamic viscosity
B_ρ	Bias limit of the fluid density
$B_{\varphi_{in}}$	Bias limit of the electrical input power to EHD pump
B_1	Bias limit due to instrument calibration
B_2	Bias limit due to data acquisition

B_3	Bias limit due to data reduction
c	Concentration of neutral species
c_0	Concentration of neutral species in thermodynamic equilibrium
dP	Total differential pressure across EHD pump
dP_f	Differential pressure across EHD pump caused by friction
dP_{net}	Differential pressure across EHD pump due to EHD effects
D_h	Hydraulic diameter
D_i	Diffusion constant of a charge of i^{th} species
e	Applied voltage
e^-	Electron
$\vec{E}$	Electric field
f_e	Force density
g	Parameter (measured quantity)
G	Rate of charge generation per unit volume
$\bar{h}$	Average heat transfer coefficient
I	Current consumed by EHD pump
I_{intek}	Current output of the mass flow meter
I_{RTD}	Current through the RTD
$\vec{j}$	Current density
k_b	Boltzmann's constant
k_f	Thermal conductivity of the face-sheet
k_l	Thermal conductivity of the fluid

l	Thickness of the face-sheet
m	Electrode metal
$\dot{m}$	Mass flow rate
M	Number of samples averaged
n_i	Number density of i^{th} species of charge carrier
n_-	Concentration of negative ions
n_+	Concentration of positive ions
N	Number of samples
$\overline{Nu}$	Average Nusselt number
P^*	Dimensionless pressure generation
$\dot{q}$	Time rate of thermal energy change
q_i	Charge of i^{th} species of charge carrier
Q	Volume flow rate through EHD pump
$Q_{total\,mL}$	Total volume flow rate
Q_{3g}	Mass flow rate in line (3)
Q_{3mL}	Volume flow rate in line (3)
r	Result (function of multiple parameters)
R	Rate of charge recombination per unit volume
RD	Voltage reading by the data acquisition unit
Re	Reynolds number through EHD pump
RG	Measurement range of the data acquisition unit
R_h	Hydrodynamic radius of a charge carrier

R_{intek}	Resistance used in calculating mass flow rate in line (3)
R_{ref}	Reference resistance used in calculating fluid temperature
S	Surface enclosing an arbitrary volume
S_{dP_f}	Precision index of differential pressure across EHD pump caused by friction
$S_{I_{RTD}}$	Precision index of the current through the RTD
S_r	Precision index of a result
$S_{\bar{r}}$	Precision index of the average of multiple results
$S_{R_{RTD}}$	Precision index of RTD resistance
S_T	Precision index of fluid temperature
$S_{V_{ref}}$	Precision index of the voltage drop across the reference resistor used in calculating fluid temperature
$S_{V_{RTD}}$	Precision index of the voltage drop across the RTD
S_X	Precision index of a sample population with *N* samples
$S_{\bar{X}}$	Precision index of the average of *M* samples
t	Student value (function of # of degrees of freedom)
T	Fluid temperature
T_c	Temperature of a satellite component
$T_{m,i}$	Mean inlet temperature
$T_{m,o}$	Mean outlet temperature
T_s	Temperature of inside surface of a fluid channel
$\vec{u}$	Flow velocity

$\vec{u}_i$	Velocity of charge of ith species
u^*	Dimensionless velocity
U	Uncertainty of a parameter
U_r	Uncertainty of a result
v	Mean flow velocity through EHD pump
V	Volume
V_{intek}	Voltage reading for mass flow meter converted from current output
V_{ref}	Voltage drop across reference resistor used in calculating fluid temperature
V_{RTD}	Voltage drop across RTD
w	Number of parameters used to calculate a result
$\bar{X}$	Average of *N* or *M* samples
X_i	Value of a sample
Y^-	Negative ion (anion)
Z^+	Positive ion (cation)
α_d	Dissociation rate coefficient
α_r	Recombination rate coefficient
ε	Fluid electric permittivity
λ	Thickness of the heterocharge layer
μ	Fluid dynamic viscosity
ρ	Fluid density
ρ_e	Net charge density
ρ_i	Charge density of ith species of charge carrier

σ	Fluid electric conductivity
τ	Charge relaxation time
φ_{in}	Electrical power consumed by EHD pump

1. Introduction

1.1. The Biologically-inspired Thermal Control System

Currently, large military satellites used for reconnaissance, communications, and tracking of friendly forces require three to ten years to develop and cost tens of millions to billions of dollars [1]. These large systems are customized to each mission and optimized to minimize mass and maximize reliability. But there is a growing need to make the United States' suite of space-based capabilities more adaptable to emerging threats and new technologies by developing the ability to field small satellites quickly and cheaply [2]. The modular satellite architecture discussed by Arrit, et al. [3] is a key development that may significantly reduce the development time and cost of satellites. These architectures are able to accommodate a wide range of mission parameters because satellite components can be quickly added or subtracted from the system as needed, and satellite subsystems can be scaled accordingly. However, a satellite subsystem which does not easily lend itself to a modular approach is the thermal control system.

The purpose of the thermal control system (TCS) is to maintain the temperatures of all electronic components within safe ranges. Traditionally, it is an optimized point design that relies primarily on passive heat transfer devices. It is the last subsystem to be designed, requiring definition of all other subsystems, the payload, and the mission orbit; it also requires extensive modeling and testing programs. Heat loads generated by electrical components and those imposed by the environment must be known. But a new TCS must be designed without complete knowledge of these parameters. Though authors such as Williams, et al. [1, 4] and Hengeveld, et al. [5-6] have attempted to bound the TCS requirements for a wide variety of missions, some parameters remain nebulous. A

possible solution to this problem discussed by Williams, et al. [7-8] is to integrate an active TCS into a new isogrid structural satellite panel. This novel TCS will accommodate a wide variety of electrical components and orbits and the associated heat loads. The isogrid structure, shown in Figure 1, consists of a series of crisscrossing ribs which resist bending. The thermal management capabilities of the panel are derived from hollowing out the ribs and using them as a coolant distribution network. Hollow ribs have a greater moment of inertia than solid ribs of the same mass, thereby providing greater stiffness and enhancing structural efficiency. A control system consisting of pumps and valves will control flow distribution throughout the panel and control the temperature to any electronic components mounted to the panel's surface. For electronics with high heat fluxes, the basic distribution network may not suffice, and smaller channels may be machined into the panel for added heat transfer area, as shown in Figure 2. This type of thermal control system is referred to as a biologically-inspired design, as it is reminiscent of the vascular systems in living organisms, where the ribs of the panel function as arteries and veins, the smaller channels as capillaries, and the pump(s) as the heart.

Traditionally, satellite thermal control systems are cold-biased, meaning that the passive heat transfer devices used are designed to prevent the overheating of components during the hottest period of orbit. This requires survival heating to prevent components from freezing during the cold phase of orbit, at a significant cost in mass and power consumption. The biologically-inspired TCS will constantly modulate the amount of heat transferred to space during all phases of orbit by actively controlling flow to and within the panels, thereby reducing or even eliminating the need for survival heating.

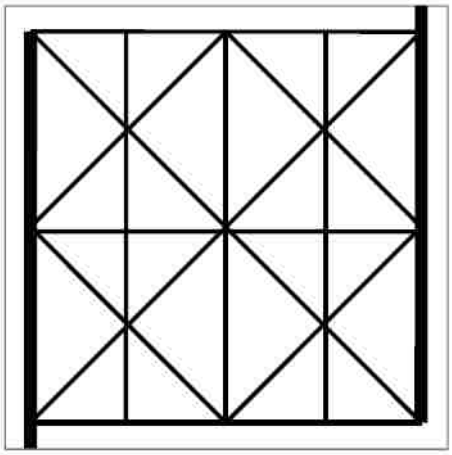

Figure 1: Isogrid rib structure of a panel [8].

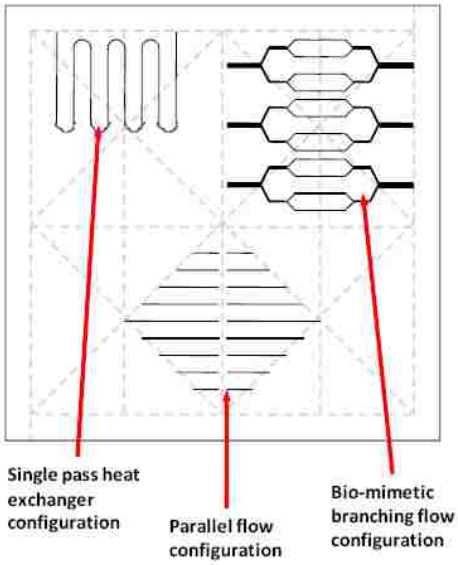

Figure 2: View of the isogrid panel showing the capillary channels in three different configurations [8].

Active thermal control systems such as pumped fluid loops are not commonly used in space because mechanical pumps typically do not offer the reliability of passive heat transfer devices. Improved or new pumping technologies are necessary to make the

biologically-inspired TCS feasible. Electrohydrodynamic pumping, which relies on electric fields to move fluids, is an attractive alternative to mechanical pumping.

1.2. Electrohydrodynamic Pumping

Electrohydrodynamics (EHD) is the study of the interaction of flow fields and electric fields. A fluid with a low electrical conductivity, when influenced by shaped electric fields, may be pumped without the use of moving parts. EHD pumps generally consist of one or more pairs of electrodes embedded in a fluid passage. A D.C. voltage applied across the electrodes permeates the fluid with an electric field, generating and transporting free space charges between the electrodes and giving rise to electrical current. The bulk fluid is dragged along with the charges, producing a net flow. The force density on a fluid permeated by an electric field is [9]

$$f_e = \rho_e \vec{E} - \frac{1}{2} E^2 \vec{\nabla} \varepsilon + \frac{1}{2} \vec{\nabla} \left[E^2 \left(\frac{\partial \varepsilon}{\partial \rho} \right)_T \rho \right] \tag{1.1}$$

where ρ_e is the net charge density of the fluid in Coulombs per unit volume, $\vec{E}$ is the electric field in volts per meter, ε is the electric permittivity of the fluid in Farads per meter, and ρ is the fluid density in kilograms per cubic meter. The first term on the right side of equation (1.1) is the Coulomb force, which acts on space charges in the electric field. The second and third terms are the dielectrophoretic and electrostriction forces, respectively. Because the fluid medium of interest is an isothermal, single-phase liquid, the dielectrophoretic force, which relies on a gradient in permittivity, and the electrostriction force, which is present only in compressible fluids, both vanish. Thus, only the Coulomb force is available for pumping.

The continuous electrical current needed by EHD pumps requires a continuous supply of charges. Three types of EHD pumping exist which differ by their mechanisms of space charge generation: ion drag pumping, induction pumping, and conduction pumping. Ion drag pumping relies on charges injected into the fluid by the electrodes. Ion drag pumping of liquids was first theoretically and experimentally investigated by Stuetzer [10], and subsequently by Pickard [11-12]. Though this type of pumping has been thoroughly studied, its potential applications are limited because the process of charge injection can degrade the electrical properties of the fluid. The pumps also require very high electric field strengths and may be hazardous to operate. Induction pumping uses a potential wave traveling perpendicular to a gradient or discontinuity in conductivity (such as that across a liquid-air interface) to induce charges in a liquid. This type of pumping was introduced in 1966 by Melcher [13] and has been used to pump liquid films for enhancement of heat transfer in Brand and Seyed-Yagoobi [14]. Seyed-Yagoobi [15] further discusses ion drag and induction pumping.

Conduction pumping, a more recent discovery, generates charge carriers by dissociation of the electrically neutral fluid into ions. This does not lead to deterioration of the fluid properties because the ions recombine once outside the electric field. This type of pumping shows promise in applications such as control and enhancement of two-phase heat transfer and control of mass transport in microgravity environments. EHD conduction pumps are ideal for space applications because they have simple, light-weight designs, they have no moving parts (no vibration, high reliability), they have fast response times, and they consume little power (several Watts).

1.3. Electric Conduction in Liquids

EHD conduction pumping may be viewed as a by-product of electric conduction in liquids. Conduction in liquids has been reviewed by Gallagher [16], Adamzewski [17], and Felici [18-19]. To understand the pumping phenomenon, one must understand how charge carriers are generated and distributed through the liquid leading to the generation of pressure.

1.3.1. Charge Conservation Equation

In a stationary volume *V* of fluid bounded by the surface *S*, the ith species of charge carrier has a number density of n_i and a unit charge of q_i. The charge density of the ith species is $\rho_i = n_i q_i$. The time rate of change of charge in the volume is determined by the net flux of charges across *S* and the rates of volumetric charge generation, *G,* and recombination, *R* [9]

$$\frac{d}{dt}\int_V \rho_i dV = -\int_S \rho_i \vec{u}_i \cdot \vec{n} dA + \int_V (G - R)\, dV \tag{1.2}$$

where $\vec{u}_i$ is velocity of the ith species of charge carrier and *G* and *R* have units of charge per unit volume per second. Using the Leibnitz rule on the left side, and applying Guass' theorem to the surface integral yields the differential form of this equation

$$\frac{\partial \rho_i}{\partial t} + \nabla \cdot \rho_i \vec{u}_i = G - R \tag{1.3}$$

Defining the current density of the ith species as $\vec{j} = \rho_i \vec{u}_i$, charge conservation may also be written

$$\frac{\partial \rho_i}{\partial t} + \nabla \cdot \vec{j} = G - R \tag{1.4}$$

In the next section, the velocity term is expanded to reveal how charges are transported inside the volume.

1.3.2. Transport of Charge Carriers

Though the fluid of interest is a liquid, the behavior of charge carriers is approximated by the ideal gas law [20]. In a fluid at rest, the velocities of the charge carriers are affected by three forces: the Coulomb force, $q_i\vec{E}$, the friction force caused by molecular collisions, given by Stoke's Law, $6\pi\mu R_h\vec{u}_i$, and the force of molecular diffusion by Fick's law, $1/n_i\,\nabla(n_i k_b T)$. Here, μ is the dynamic viscosity of the fluid, R_h is the hydrodynamic radius of the charge carrier, k_b is Boltzmann's constant, and T is the absolute fluid temperature. Assuming the ion, once acted upon by these forces quickly attains terminal drift velocity, there is a balance between the friction, Coulomb, and diffusion forces [20]

$$6\pi\mu R_h\vec{u}_i = q_i\vec{E} + \frac{1}{n_i}\nabla(n_i k_b T) \tag{1.5}$$

The velocity of the i[th] charge carrier is then

$$\vec{u}_i = b_i\vec{E} + D_i\nabla n_i \tag{1.6}$$

where b_i is introduced as the charge mobility, and D_i is the diffusion coefficient

$$b_i = \frac{q_i}{6\pi\mu R_h} \qquad D_i = \frac{k_b T}{6\pi\mu R_h n_i} \tag{1.7}$$

Motion of charges caused only by the Coulomb force is referred to as charge migration, and the term $b_i\vec{E}$ is called the migration term. If the fluid is not at rest but is given a velocity $\vec{u}$, then charges are advected with the fluid, adding a third contribution to the charge velocity

$$\vec{u}_i = b_i\vec{E} + D_i\vec{\nabla}n_i + \vec{u} \tag{1.8}$$

Inserting the new expression for charge velocity into the charge conservation equation (1.3) yields

$$\frac{\partial \rho_i}{\partial t} + \nabla \cdot \rho_i \left[b_i \vec{E} + D_i \nabla n_i + \vec{u} \right] = G - R \tag{1.9}$$

This equation gives *i* scalar expressions describing the distributions of *i* charge species and the electric field, $\vec{E}$. The mobility constant b_i and the diffusion coefficient D_i, which both stem from thermal particle motions, are related by the Einstein relation [9]

$$\frac{D_i}{b_i} = \frac{k_b T}{q_i} \tag{1.10}$$

For a carrier of charge e = 1.602 x 10^{-19} Coulombs, a fluid temperature of 295 K, and the Boltzmann constant, k_b= 1.381 x 10^{-23} J/K, the ratio is

$$\frac{D_i}{b_i} = \frac{1}{40}\ volts \tag{1.11}$$

so that when the potential exceeds 250 volts, diffusion contributes less than 0.1% of the charge velocity and becomes negligible.

1.3.3. Generation of Charge Carriers

Charge carriers are either electrons or ions. Electrons usually do not contribute to conduction in a liquid since they exist for a very short time; they are quickly trapped by impurities or by molecules of the bulk fluid. Ions are generated either by dissociation of impurities in the fluid, by dissociation of the fluid itself, by injection by a corona source, or by electrochemical reactions at the electrode-liquid interface [20]. Often, ions that enter the liquid become solvated, meaning they are surrounded by a cloud of molecules which adhere to the ion by dipolar forces. Ions that escape recombination are neutralized by the transfer of electrons at the electrodes, thus allowing for continuous current.

Cations, Z^+, are discharged at the cathode by accepting an electron e^- from the metal surface in a reduction reaction

$$Z^+ + e^- = Z \tag{1.12}$$

and anions, Y^-, are discharged at the anode by donating an electron in an oxidation reaction

$$Y^- = Y + e^- \tag{1.13}$$

1.3.3.1. Dissociation and Recombination

The reversible dissociation-recombination reaction [20]

$$ZY \xleftrightarrow{\alpha_d,\ \alpha_r} Z^+ + Y^- \tag{1.14}$$

separates electrically neutral species ZY into free cations Z^+ and anions Y^-, where α_d and α_r are the dissociation and recombination rate coefficients, respectively. Neutral species may be individual liquid molecules, groups of liquid molecules, or pairs of solvated impurity ions associated by the Coulomb force. If c is the concentration of neutral species, and n_+ and n_- are the concentrations of positive and negative ions, then at any moment [20]

$$-\frac{dc}{dt} = \alpha_d c - \alpha_r n_+ n_- = \alpha_d c - \alpha_r n_i = G - R \tag{1.15}$$

since anions and cations are always created in pairs. Even in the absence of an electric field, pairs of ions as well as free ions will often exist in a fluid in various concentrations depending on the polarity, or relative electric permittivity ε, of the fluid. Polar liquids, which tend to have relative permittivities greater than 2 at room temperature, will naturally dissociate all impurities into ions which remain unbound, while non-polar liquids, characterized by relative permittivities less than 2, will create a dynamic

equilibrium between the rates of dissociation and recombination. In thermodynamic equilibrium

$$\alpha_d c_0 = \alpha_r n_+ n_- = \alpha_r n_i \tag{1.16}$$

where c_0 is the equilibrium concentration of neutral species. But, as discussed by Onsager [21], application of a sufficiently strong electric field increases the local rate of dissociation while the rate of recombination is almost unaffected, hence increasing the local concentration of ions. This field-enhanced dissociation, together with increased drift velocities, may increase the current by several orders of magnitude.

1.3.3.2. Ion Injection

At high field strengths, a second mechanism of charge generation, ion injection at the electrode-liquid interface, may appear. Ions may be injected by means of a corona source or by electrochemical reactions. Corona discharges typically occur at sharp points or edges on the electrodes, where the electric field is concentrated enough to form a small conductive region in the fluid but insufficient to cause complete breakdown or allow arcing to adjacent conductors. In this region, electrons emitted by the positive electrode are accelerated by the electric field and collide with neutral molecules, forming positive ions and liberating more electrons (called electron avalanche). These ion-electron pairs then drift apart because of Coulomb forces, preventing recombination. The additional electrons seed further avalanches and the resulting positive ions drift toward the ground electrode, giving rise to current. Here, sources of electrons are thought to be the Schottky effect or field emission (electron tunneling).

Chemical reactions at the electrode-liquid interface involve an exchange of electrons between fluid ions and the electrode surface that is mediated by the electric double layer, shown in Figure 3.

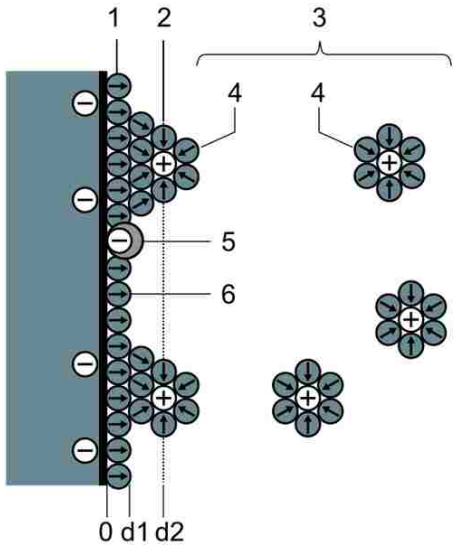

Figure 3: Structure of the electrode-liquid interface of an anode: (1) Inner Helmholtz layer (2) Outer Helmholtz layer (3) Diffuse layer (4) Solvated cations (5) Impurity anion (6) Solvent anion [22].

Layer (1) is the inner Helmholtz layer, composed of fluid ions and ion pairs absorbed by the metal, and it has the same polarity as the metal. The outer Helmholtz layer (2) is composed of solvated fluid ions with charge opposite the electrode. The outermost layer (3) is a region of charge opposite that of the electrode called the diffuse layer, which is loosely attracted to the electrode by Coulomb forces. The exchange of electrons through these charged layers occurs by oxidation-reduction reactions that inject ions into the liquid bulk. The electron donor molecule *Z* in liquid phase releases an electron, which is collected by the metal *m*, and a positive ion is released directly into the liquid [20]

$$m + Z \overset{oxidation}{\underset{reduction}{\longleftrightarrow}} m(e^-) + Z^+ \tag{1.17}$$

For further explanation of injection reactions, see Felici [23] and Alj, et al. [24]. If the injection reaction changes the chemical composition of the products, the original substances cannot be regenerated when ions are neutralized, and any EHD pumping effects will not be repeatable. Impurities in the liquid such as water or oxygen, or an electrode material that is not chemically neutral may cause non-regenerative reactions.

1.3.4. Current-Field Characteristic

According to Gallagher [16], the current-field characteristic of a liquid may include regions of low-field (<0.1 MV/m), intermediate-field (~2 MV/m), and high-field (up to 100 MV/m) intensities, as shown in Figure 4. In the low-field region (1), the electric field is not strong enough to appreciably modify the equilibrium rate of ion generation, so the current density is linear with field strength (Ohmic), $\vec{j} = \sigma\vec{E}$, where σ is the conductivity of the fluid. In this region, dissociated impurities are thought to be the primary source of free charges. In region (2), as the field intensifies further, drift velocities increase to the point that current is limited either by the rate of generation or the rate of neutralization at the electrodes. This is called saturation. Thus the current increases only slightly with field strength, and the characteristic is sub-Ohmic. In this case, layers of space charge may gather around the electrodes. At high field strengths in region (3), current increases rapidly and breakdown may occur. This characteristic is always observed in gasses but may be ill-defined or not present in liquids. Depending on the properties of the fluid and the geometries and surface finish of the electrodes, field-enhanced dissociation or ion injection may onset in the Ohmic or sub-Ohmic regimes, changing the shape of the characteristic from Figure 4.

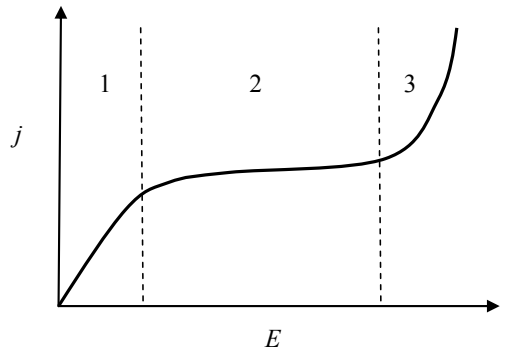

Figure 4: Three regions of the current-field characteristic: (1) low-field region, (2) intermediate-field region, (3) high-field region [16].

1.4. The EHD Pumping Mechanism

In the conduction processes described above, free ions which escape recombination travel along the electric field lines and gather in the diffuse layers surrounding the positive and negative electrodes. This layer is also referred to as the heterocharge layer since its polarity is always opposite to that of its adjacent electrode. If the electrodes are properly shaped, the distribution of Coulomb force, equation (1.1), between the heterocharge layers and their adjacent electrodes is unbalanced, resulting in a net flow. Many electrode designs have been studied, each falling into one of two groups: penetrating electrode designs and flush electrode designs. Figure 5 shows the two configurations along with heterocharge layers and arrows indicating the fluid attraction towards the electrodes.

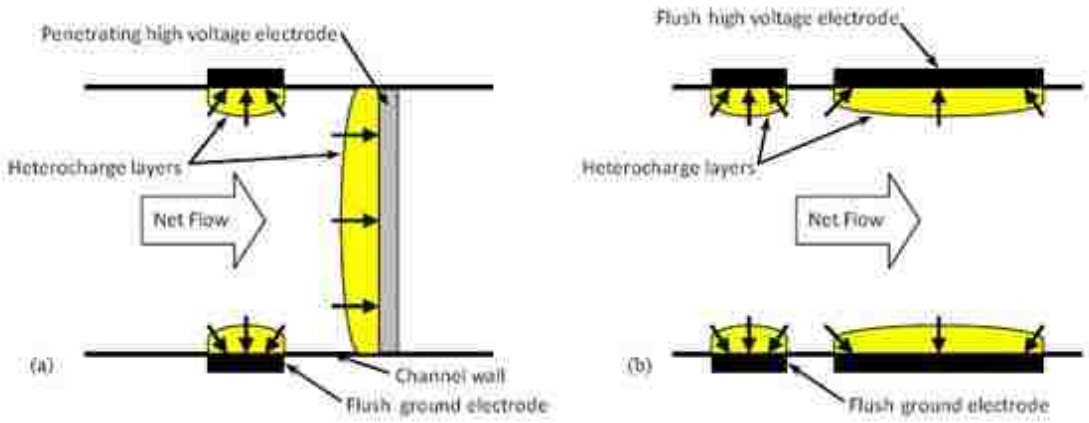

Figure 5: Schematic showing (a) a pair of penetrating type of electrodes and (b) a pair of flush type electrodes [25].

Penetrating electrode designs may consist of pins, rings, or perforated discs inserted into the flow path. These designs tend to have higher efficiencies and are capable of generating higher differential pressures than flush electrode designs. Pearson and Seyed-Yagoobi [26] presented several illustrations of these designs. Flush electrode designs rely on the difference in thicknesses between ground and high voltage electrodes to create non-symmetric heterocharge layers and a net flow. Flush designs have been studied as means of pumping fluid films [27] and are more easily built on small scales than penetrating electrode designs. Increasing the voltage applied across the electrodes results in thicker heterocharge layers and increased pressure generation. Pressure also increases linearly with the number of electrode pairs as in a multistage pump.

2. Literature Review and Experimental Objectives

2.1. Review of Related Literature

Williams, et al. [7] presented the concept and preliminary analysis of an isothermal panel used in the biologically-inspired thermal control system. Primary fluid supply channels (arteries) and sub-supply channels are integrated into the panel by hollowing out the ribs of the isogrid structure, and small face-sheet channels (capillaries) are machined into the front of the panel base plate. Figure 6 shows the isogrid rib architecture and fluid supply channels on the left and face-sheet channels on the right. The arteries provide a large cross-sectional area for large flow rates, while the capillaries provide additional heat transfer area for the fluid. As illustrated in Figure 7, waste heat from subsystem components mounted to the face-sheet is transferred to the fluid in the capillaries, pumped to radiating surfaces to be cooled, and returned to the face-sheet via the arteries. Thermally-coupled paraffin valves were proposed to control fluid distribution in the panel. Structural analysis of the panel showed that the hollow rib design should improve the structural efficiency of the panel compared to solid ribs with the same mass, and thermal analysis showed that adequate cooling of the face-sheet can be achieved without excessive pressure loss through the system.

Lyall, et al. [28] described the first prototype isothermal panel, and testing showed that the integrated thermal control system provides satisfactory thermal management for standard satellite bus components. A single panel with isogrid rib structure and a serpentine face sheet channel was machined from a single piece of aluminum. Chilled water was pumped through the face sheet channel while a heat flux was applied to the face sheet. The temperature distribution on the face sheet was

measured for various applied heat fluxes. The panel removed 70 W of waste heat for 0.02 W of pump input power.

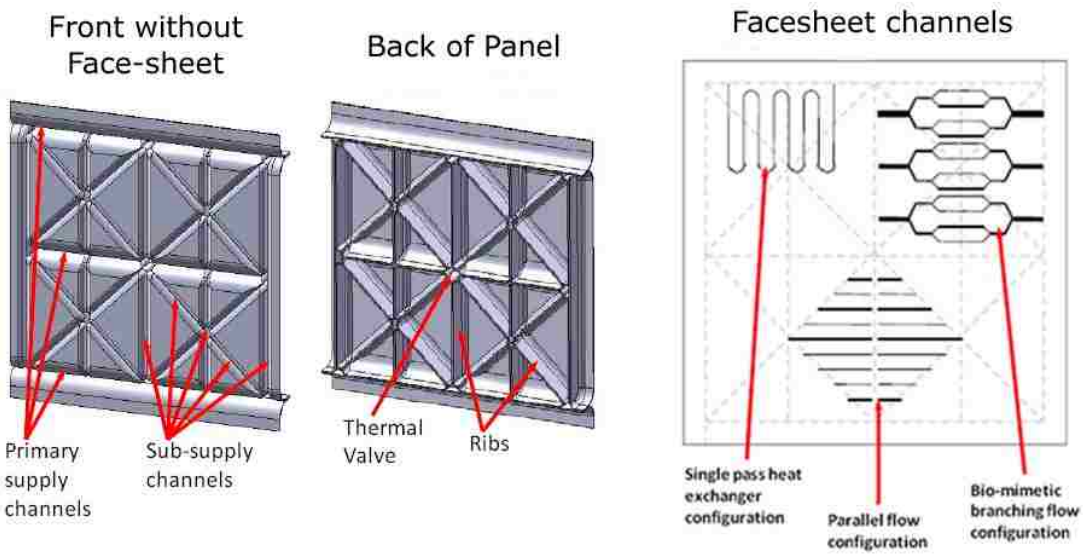

Figure 6: Models of the isothermal panel, which integrates fluid channels into the rib structure and face-sheet [8].

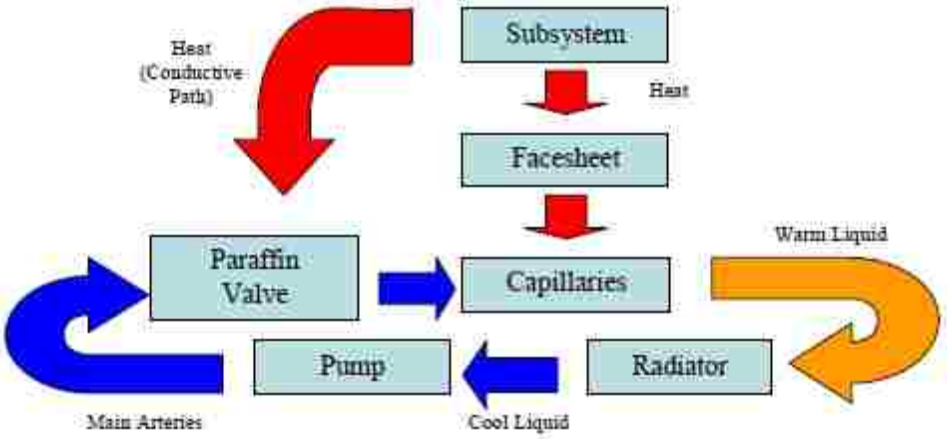

Figure 7: General thermal schematic for the biologically-inspired TCS [8].

A parametric study performed by Williams et al. [8] determined the optimum dimensions of the sub-supply channels of the multifunctional panel. Proposed manufacturing methods for composite multifunctional panels create a roughly triangular rib cross-section, shown in Figure 8. By considering heat transfer capability, pressure drop in the system, and face-sheet rigidity, the optimum rib radius was selected as 7.6 mm.

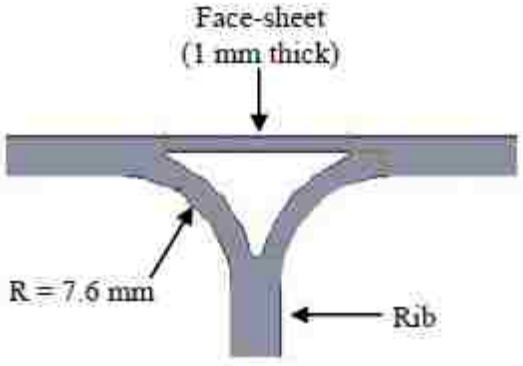

Figure 8: Flow cross-section of a sub-supply channel [8].

Jeong and Didion [29-30] characterized the performance of an EHD driven two-phase thermal control system that consisted of an EHD conduction pump, condenser, pre-heater, evaporator, transport lines, and reservoir. This work confirmed that the pressure rise across the pumps increases with applied voltage. The paper also presented the effects of air mixed in the working fluid and variation in fluid temperature. The pumps were operated at voltages ranging from 0 to 20 kV and currents ranging from 0 to 200 μA. The EHD pump operated the two-phase loop despite pressure oscillation caused by boiling in the evaporator and provided recovery from evaporator dry-out when the applied voltage was increased. The apparatus was able to remove more than 100 W of heat for approximately 3 W of pump input power.

Feng and Seyed-Yagoobi [31] demonstrated the successful control of liquid flow distribution between two branch lines using an EHD conduction pump. An EHD pump was installed in one of two parallel branches of a mechanically driven fluid loop with mass fluxes of 100 and 200 (kg/s)/m^2. The pump was operated at voltages of 10 and 15 kV, and current consumption remained below 100 μA. When activated, the pressure generated by the EHD pump increased the flow rate in its branch. At an applied voltage of 15 kV and a total mass flow rate of 100 (kg/s)/m^2, the EHD pump pushed all fluid flow through its branch, leaving the other branch with zero flow.

Pearson and Seyed-Yagoobi [25] presented the fabrication and testing of a flush electrode, micro-scale EHD pump. The fluid passage and electrode spacing were an order of magnitude smaller than those of previous studies. The fluid passage was a 1 mm x 15 mm rectangular channel, and the gap between the high voltage and ground electrodes pair was 250 μm. Tests were conducted at applied voltages ranging from 0 to 4 kV. The pump consisted of stacked discs, each containing a cut-out of the fluid passage, alternating between metal electrode layers and insulating layers all of suitable thicknesses. Referring to Figure 5b on page 14, a thick electrode layer in the micro-scale pump corresponds to a high voltage electrode in the schematic and a thin electrode layer to a ground electrode. The pump generated 390 Pa pressure rise at a voltage of 4 kV while consuming 21 μA.

Feng and Seyed-Yagoobi [32] published a theoretical model of EHD conduction pumping which reveals energy conversion processes, including effects of ion convection on pumping performance. According to this model, flow in the vicinity the electrodes affects pump performance by changing the distribution of ions near the electrode

surfaces. The electric conduction process between the two parallel plate electrodes was simulated, and the anode alone is shown in Figure 9. This is an idealized electrode structure that occupies 100% of the flow cross-section yet causes no pressure drop or turbulence. The work showed that the flow, $\vec{u}$, in the positive direction carries charges away from the conducting surface of the electrode, which results in a thicker heterocharge layer.

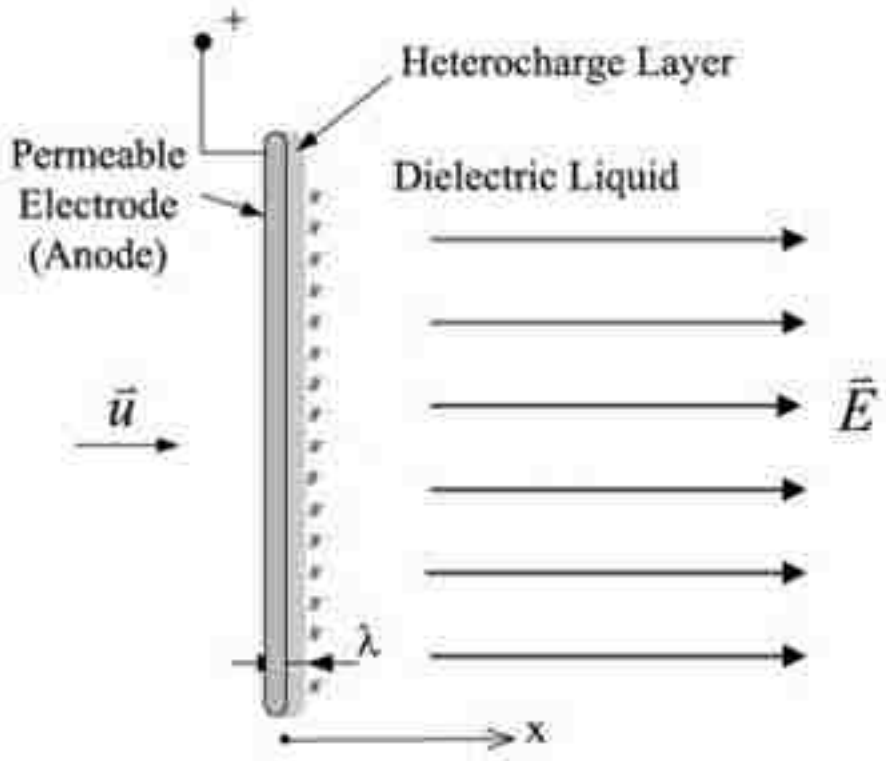

Figure 9: A fully permeable plate electrode [32].

A thicker heterocharge layer results in greater Coulomb forces and greater pressure generation. Pressure generated by the electrode in Figure 9 would normally motivate flow

in the negative x direction. In this scenario, as flow velocity increases, the pressure generation should decrease as shown in Figure 10.

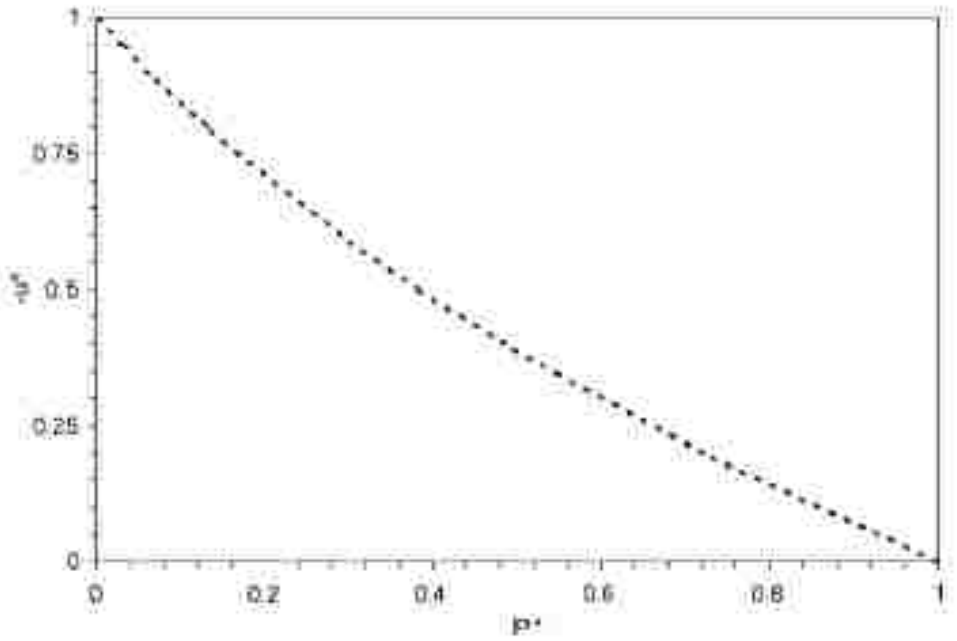

Figure 10: Non-dimensional flow velocity vs. normalized pressure generation [32].

The ordinate of the plot is a dimensionless velocity, $u^* = \frac{\vec{u}\lambda}{eb}$, where $\vec{u}$ is the flow velocity, λ is the heterocharge layer thickness, e is the applied voltage, and b is the ion mobility of the fluid. The dimensionless velocity, u^*, can be thought of as the ratio of the flow velocity, $\vec{u}$, to the ion drift velocity, $\frac{eb}{\lambda}$. This ratio is plotted against normalized differential pressure, $P^* = \frac{\Delta P(U \neq 0)}{\Delta P(U=0)}$, where the numerator is the differential pressure at non-zero flow velocity, and the denominator is the differential pressure at zero flow velocity. Note from the plot that when the flow velocity equals the ion drift velocity,

$u^* = 1$, zero pressure is generated. Physically, this means that the flow removes the heterocharge layer from electrode surfaces and prevents additional pressure generation.

In a later study, Yazdani and Seyed-Yagoobi [27] modeled various Coulomb force distributions and 2D flow fields around a pair of flush electrodes. The difference in thickness between the ground and high voltage electrodes creates an asymmetric Coulomb force distribution resulting in a net flow from right to left as well as vortex-like circulations near the electrodes, as shown in Figure 11. It was found that the net flow created by flush electrodes always proceeds from the thin electrode to the thick electrode regardless of their electrical polarity. The effects of the horizontal and vertical velocity components of the flow on the shape of heterocharge layers were investigated. The horizontal component of flow generally suppressed the formation of heterocharge layers, which decreases pressure generation. The vertical component enhanced formation when directed away from the electrodes and suppressed formation when directed toward the electrodes. Ultimately, greater net flow velocities in the negative x direction reduced the sizes of the heterocharge layers on both electrodes and thereby reduced pressure generation.

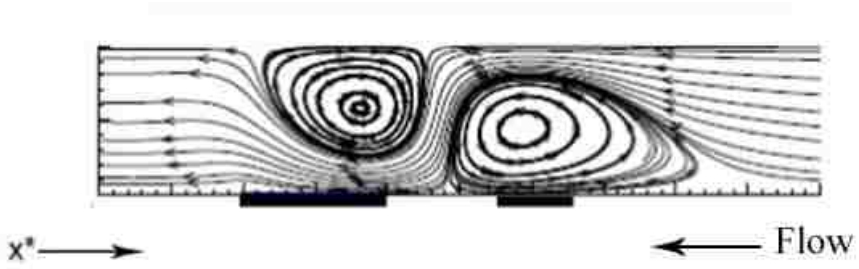

Figure 11: Flow field near a pair of flush electrodes, adapted from Yazdani and Seyed-Yagoobi [27].

EHD pump performance is also highly dependent on fluid properties. Crowley et. al. [33] created a simple model of EHD pumping which shows that high electric permittivity, ε, and low viscosity lead to high flow velocities, and that low conductivity, σ, and charge mobility, b, lead to high efficiencies. High permittivity and low conductivity result in a large charge relaxation time, $\tau = \varepsilon/\sigma$, which is the amount of time an ion maintains its charge in an electrically neutral medium. Longer relaxation times enable thicker heterocharge layers to form, leading to greater pressure generation. Low conductivity and mobility indicate low charge drift velocities, meaning that EHD effects cause the fluid to move at nearly the same speed as the charges. The effects of flow regime (laminar or turbulent) on performance were also derived. The result is a set of restrictions on an EHD pump design that mandate that flow velocity must be high enough to avoid conduction and mobility losses but is limited by viscosity, turbulence, and maximum electric field strength before breakdown.

2.2. Summary and Experimental Objectives

Previous work has demonstrated that the biologically-inspired thermal control system (TCS) can control the temperature on the face-sheet of an isogrid multifunctional panel and thereby adequately control the temperature of standard satellite bus components. A growing body of work characterizes EHD pump performance in single-phase heat transfer experiments and flow distribution experiments. Various heat transfer experiments show that an EHD pumped fluid loop can be used as a stand-alone system for thermal management, and previous flow distribution studies show the feasibility of using EHD pumps to prevent maldistribution of fluid flow. Also, EHD pumps can be sized to the micro-scale, the same scale as the sub-supply channels and capillaries in the

biologically-inspired TCS concept. Finally, theoretical modeling of EHD pumping shows that flow conditions near the electrodes significantly affect pressure generation and efficiency.

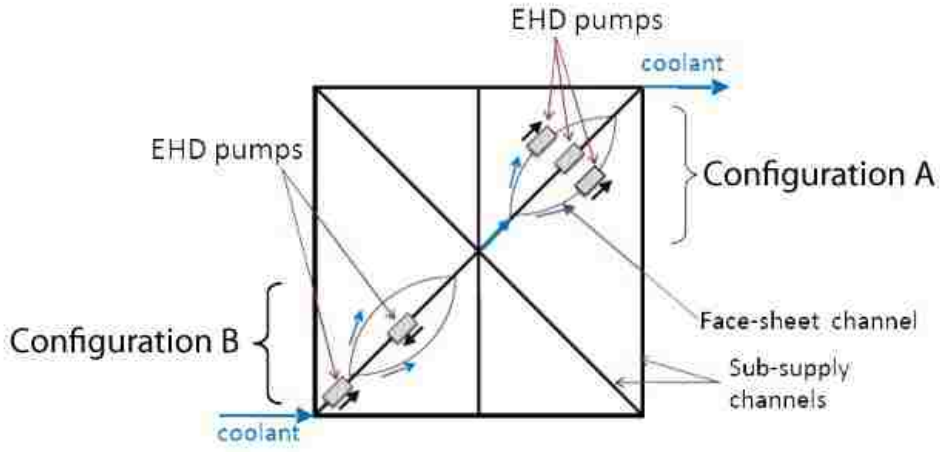

Figure 12: Illustration of possible sub-supply channel and face-sheet channel arrangements and pump locations.

However, further investigation of EHD conduction pumping is necessary before attempting integration into a satellite panel. First, no electrode designs exist that fit the shape of the sub-supply channels in the biologically-inspired TCS. This calls for characterizing the performance of an EHD pump with the unique cross-section shape of the channels. Second, EHD pumps have not been used to slow or stop fluid flow for the purpose of flow distribution control. In previous work [31], an EHD pump modified the natural distribution of fluid in parallel lines by pulling additional fluid through the desired line, such as in configuration A of Figure 12, where the pumps are located in the lines in which additional flow is desired. In other work [7-8], one large pump provides pressure

head for the whole fluid network, and passive, thermally coupled valves are suggested as a means of controlling flow distribution in the panel. These valves may be replaced by EHD pumps imposing pressures opposite to the natural flow directions on several branch lines to direct flow. Configuration B in Figure 12 shows a sample arrangement of channels in which a single EHD pump acts as a variable resistance valve by pumping in the direction opposite the natural flow direction in the sub-supply channel to direct flow through adjacent face-sheet channels. The effects of flow velocity on pump performance for this flow condition are unknown.

Based on these needs, the following research objectives were proposed:

1. Characterize the performance of a flush electrode EHD pump with the cross-sectional geometry of the sub-supply channels (Figure 8) and with the flow conditions of configurations A and B in Figure 12.
2. Demonstrate that flush electrode EHD pumps can reroute flow to a parallel line by imposing a pressure drop in an adjacent line (configuration B of Figure 12). Compare pump performance in this case to performance in a case where an EHD pump pulls additional flow through the desired parallel line (configuration A of Figure 12).

3. Experimental Method

3.1. Experimental System

3.1.1. System Configurations

The system designed to accomplish the two experimental objectives is shown Figure 13.

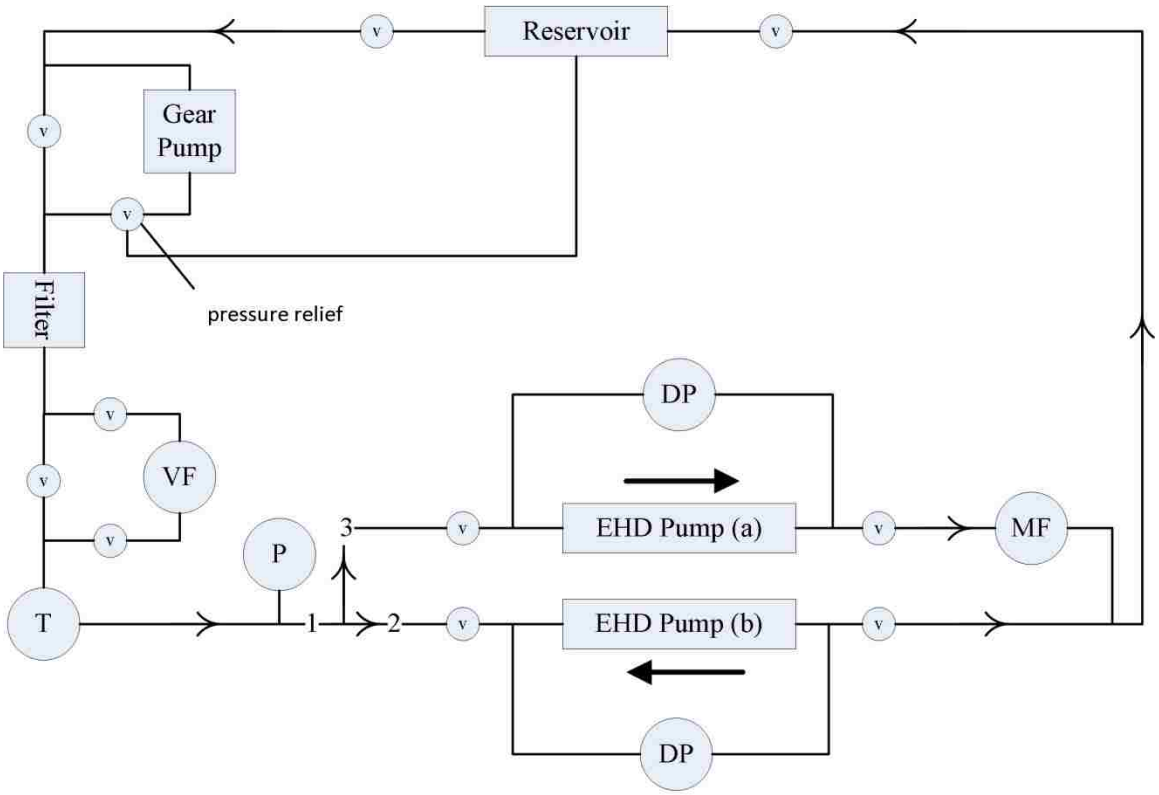

Figure 13: Illustration of the experimental system.

The system consisted of a fluid loop that was pumped by a gear pump. Fluid lines were ¼" stainless steel tubing and polyethylene hose connected by compression fittings. Flow from line (1) branched into lines (2) and (3) in the directions shown by the arrows. Two identical EHD pumps were placed in lines (2) and (3) and used to modify the distribution of flow between the lines. In line (3), EHD pump (a) pumped in the same direction as the flow velocity, and in line (2), EHD pump (b) pumped in the direction opposite to the flow velocity. Arrows next to each EHD pump indicate the direction in which EHD forces acted. Referring to objective #1, the performance of the EHD pumps under the flow conditions of configuration A from Figure 12 can be measured by setting the total flow rate with the gear pump and using pump (a) to pull additional flow through line (3) while pump (b) is idled. Similarly, configuration B from Figure 12 can be studied by setting the total flow rate with the gear pump and using pump (b) to restrict flow in line (2) while pump (a) is idled. As shown in the results chapter, the performance of EHD pump (b) in static tests was inferior to that of EHD pump (a). Consequently, comparing the performances of pumps (a) and (b) to evaluate the merits of configurations A and B in these two types of tests was impractical. To overcome this problem, only pump (a) was used in flow distribution tests, and its position and orientation with respect to flow velocity was switched with pump (b) as necessary. Because the pumps were identical, pressure losses across the pumps due to friction were equal, and also not affected by the direction of flow through the pumps. The setup pictured in Figure 13 is hereafter referred to as configuration A, and configuration B has the positions of the two EHD pumps switched. Figure 14 illustrates both configurations side by side.

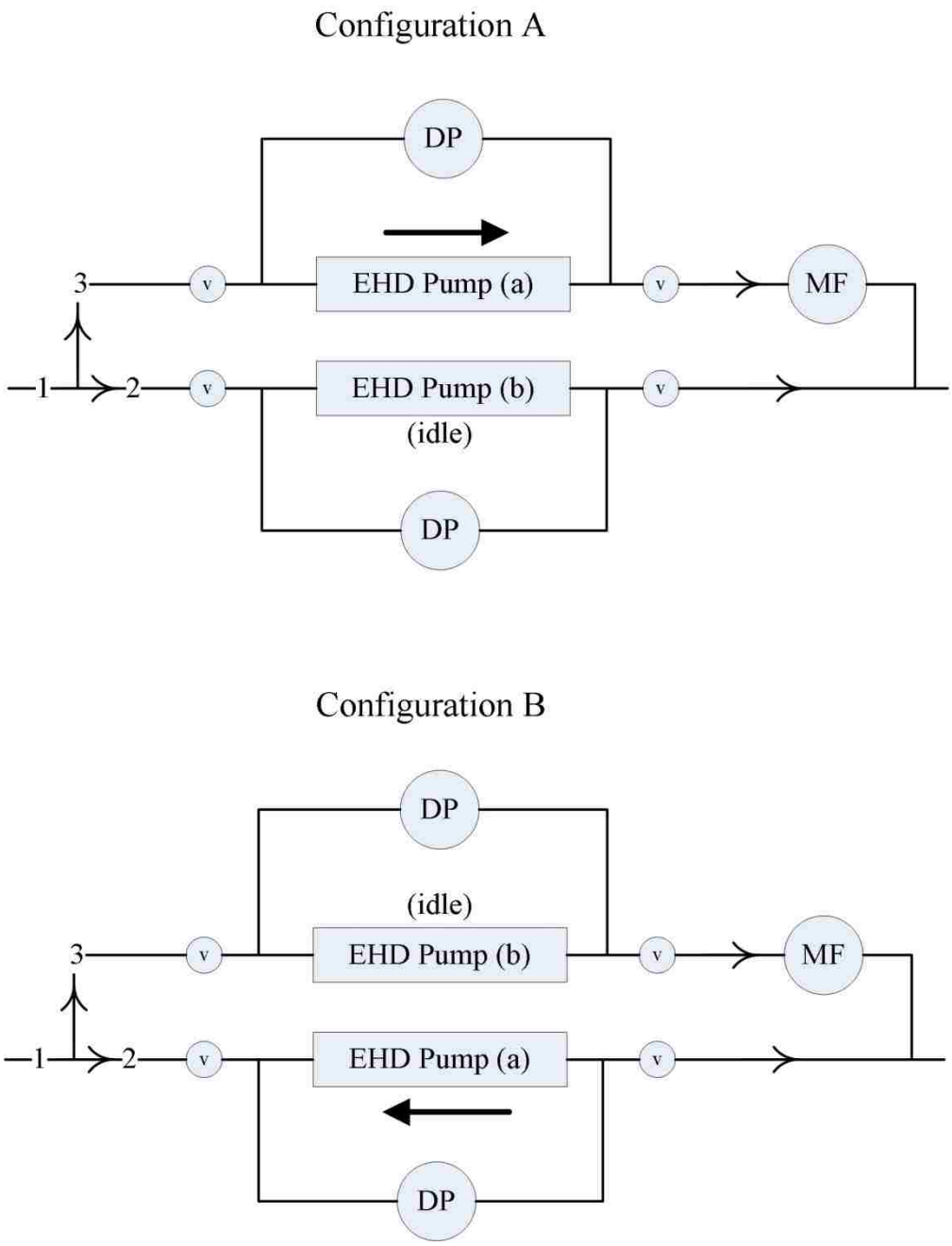

Figure 14: System configuration A (top) and configuration B (bottom).

3.1.2. Selection of the Working Fluid

Establishing the working fluid and flow rates for the system was problematic because of the interdependence of fluid properties and necessary flow rates and the

undefined configurations of the satellite and thermal control system. Satellite panel sizes, face-sheet channel geometries, face-sheet heat flux distributions, and component operating temperatures are all undetermined. The working fluid was chosen first because the number of options was quickly reduced to only three by considering the required operating temperature range (-60°C to 90°C), the electric conductivity (10^{-8} to 10^{-11} S/m), and material compatibility with Hexel 8552 and Sytech 977-2 carbon fiber resins. Novec 7600, with properties listed in Table 1, was chosen because of its relatively high electric permittivity. Two other candidate working fluids are listed in the table. The lower specific heat and thermal conductivity of Novec compared to the other liquids would provide inferior heat transfer performance; however, based on Feng and Seyed-Yagoobi [32], Novec's higher electric permittivity may sufficiently enhance pressure generation to cancel out these effects and provide superior overall system performance. The affects of the thermodynamic properties on performance, while known qualitatively, are impossible to quantify because the panel TCS configuration is not defined. Once the panel configuration is defined, studies may determine which fluid will provide the best ratio of power required by the EHD pumps to time rate of thermal energy removal from the panel.

Table 1: Electrical and heat transfer properties of three candidate working fluids

Properties @ 25 °C	Electric Permittivity	Dielectric Constant	Density	Dynamic Viscosity	Specific Heat	Thermal Conductivity
Units	Farads/m		kg/m^3	Pa*s	J/kg-K	W/m-K
Novec 7600	5.66E-11	6.4	1540	1.65E-03	1319	0.071
Paratherm CR	2.29E-11	2.6	831	9.14E-04	1989	0.139
Collanol 20	2.21E-11	2.5	886	3.40E-03	1966	0.117

3.1.3. Determination of the System Flow Rates

The system flow rate should represent the needs of a biologically-inspired thermal control system. Though some aspects of the EHD pump design are constrained by available space in a panel and by the need to use flush electrodes (discussed in section 3.2), necessary flow rates were checked against a rough heat transfer analysis of a multifunctional panel. The total flow rate for the experimental system was estimated by performing an energy balance on a panel using the average heat flux from standard electronic components, standard electronics operating temperature ranges, the properties of Novec 7600, and prospective face-sheet channel configurations and EHD pump locations. The simplest form of the steady-flow thermal energy equation is

$$\dot{q} = \dot{m} c_p \left(T_{m,o} - T_{m,i} \right) \tag{3.1}$$

where $\dot{q}$ is the time rate of thermal energy change in the fluid, $\dot{m}$ is the mass flow rate, c_p is the heat capacity at constant pressure, $T_{m,o}$ is the mean outlet temperature of the fluid, and $T_{m,i}$ is the mean inlet temperature of the fluid. This assumes that heat capacity is constant over the temperature range of the fluid. Newton's law of cooling relates the mean fluid temperature to the temperature of the inside face-sheet surface (surface contacting the fluid)

$$\dot{q} = \bar{h} A_w \left(T_s - T_{m,o} \right) \tag{3.2}$$

where $\bar{h}$ is the average heat transfer coefficient, A_w is the wetted area, and T_s is the temperature of the inside face-sheet surface. Assuming that the flow is thermally and hydrodynamically fully developed makes the heat transfer coefficient constant. The heat transfer coefficient depends on the thermal conductivity of the liquid, k_l, the hydraulic

diameter of the channels, D_h, and the average Nusselt number for fully developed laminar flow, $\overline{Nu}$

$$\bar{h} = \frac{k_l \overline{Nu}}{D_h} \tag{3.3}$$

Finally, the temperature of the inner surface of the face-sheet is related to the temperature of the outer surface (also component temperature) by Fourier's equation of conduction

$$q = -k_f A_w \frac{T_s - T_c}{l} \tag{3.4}$$

where k_f is the thermal conductivity of the face-sheet, T_c is the temperature of the outside face-sheet surface (same as component temperature), T_s is the temperature of the inside face-sheet surface from the previous equation, and l is the face-sheet thickness. The hottest fluid and component temperatures are assumed to occur near the outlet of the panel. Given a fluid inlet temperature and a maximum component operating temperature, one can determine temperature on the inner surface of the face-sheet from equation (3.4), the fluid mean temperature at the outlet of the panel from equation (3.2), and the corresponding flow rate from the thermal energy equation (3.1). The results are shown in Table 2.

We assume that all the excess thermal energy must be transferred into the fluid and none is conducted or radiated away, giving a worst case. Incidentally, the face-sheet channels and sub-supply channels have almost equal hydraulic diameters of 2.67 mm and 2.54 mm, respectively. This allows use of the same average Nusselt number for both geometries and makes the wetted area the sum of contributions from the sub-supply channels and face-sheet channels. An average Nusselt number of 5.39 is that for laminar

flow in an infinitely wide channel which is insulated on the bottom and has a constant heat flux applied to the top. This is the closest representation of the panel flow geometry readily available [34], assuming the heat flux into the face-sheet channels from below is negligible because of the low thermal conductivity of the carbon fiber reinforced polymer material.

Table 2: Fluid temperatures, fluid flow rates, and sample thermal control system parameters using Novec 7600.

Parameter		Units	
Average heat flux		W/m^2	2000
Face-sheet area		m^2	0.09
Power into the face-sheet	$\dot{q}$	W	185
Wetted area	A_w	m^2	0.03
Face-sheet thickness	l	m^2	0.001
Face-sheet thermal conductivity	k_f	W/m-K	0.60
Max component temperature	T_c	K	313
Channel surface temperature	T_s	K	303
Average Nusselt number	$\overline{Nu}$		5.39
Hydraulic diameter	D_h	mm	2.60
Fluid thermal conductivity	k_l	W/m-K	0.071
Average heat transfer coefficient	$\bar{h}$	W/m^2-K	147
Mean fluid outlet temperature	$T_{m,o}$	K	261
Mean fluid inlet temperature	$T_{m,i}$	K	260
Mass flow rate per pump	$\dot{m}$	g/s	7.23
Volume flow rate per pump		ml/min	282

Notice the high temperature differences $T_s - T_c = 10\ K$ and $T_s - T_{m,o} = 42\ K$. These are a result of the low thermal conductivities of the composite material and Novec fluid and the high heat flux. The thermal conductivity through the thickness of a composite layup with 0/±45/90° carbon fiber orientation is used [35]. A maximum component temperature T_c = 313 K and a minimum fluid inlet temperature $T_{m,i}$ = 260 K are conservative selections from the published electronics operating temperature range of

253-323 K [36]. An average heat flux of 2000 watts per square meter is used, and the face-sheet area is approximately one square foot. The wetted area of 0.03 square meters assumes that one third of the face-sheet area is wetted from underneath. The resulting flow rate of 282 milliliters per minute is equal to the total flow rate required by the panel divided by 24, as twenty four pumps will be necessary to implement the flow pattern of configuration B from Figure 12 on every sub-supply channel segment in the panel. This flow rate is used in the pump design discussed in section 3.2 and is consistent with the laminar flow assumption in the sub-supply channels but not in the face-sheet channels. Note that in a real panel, local heat fluxes may be higher than the average, requiring higher flow rates. A wide range of flow rates and mean outlet temperatures can be calculated through the analysis described above by changing fluid inlet temperature, component temperature, Nusselt number, wetted area, face-sheet channel geometries, heat flux, and pump locations. The numbers listed in Table 2 are those of only one of many possible TCS configurations and were selected because they produce a relatively high flow rate per EHD pump and are close to a worst case scenario. It is recognized that modeling, simulation, and trade studies are needed to adequately determine the optimum flow paths the operating parameters of the biologically-inspired TCS, which should be the subject of additional work.

3.1.4. Instrumentation

The pump that drove the experimental system was a Micropump GA Series magnetically-coupled gear pump with a displacement of 92 microliters, and with flow and pressure ranges of 0 - 550 mL/min and 0 – 5 bar, respectively. The magnetic coupling between the drive and the pump head prevented fluid leaks past dynamic seals,

and the small displacement produced nearly pulseless flow. Some pressure and flow pulsation was observed at low pump speeds but disappeared when pump speed was increased, as shown in Figure 15.

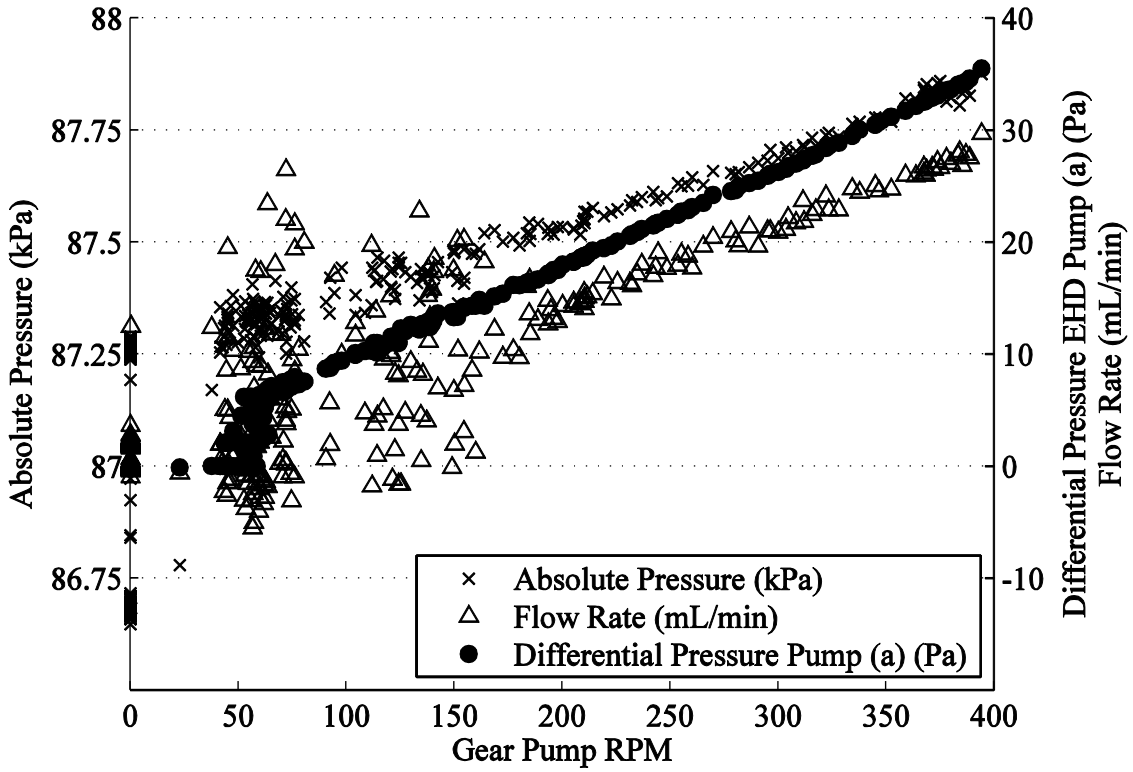

Figure 15: Absolute pressure, flow rate, and differential pressure for EHD Pump (a) vs. RPM of the gear pump.

The absolute pressure, temperature, and volume flow rate of the fluid were measured in line (1) before the flow branched to lines (2) and (3). Fluid temperature was measured by a 100 Ohm resistive temperature detector (RTD) immersed in the fluid. Because the data acquisition system could measure voltage only, the voltage drop across the RTD, V_{RTD}, for a known current, I_{RTD}, was recorded instead and used to calculate resistance and fluid temperature; I_{RTD} was calculated by taking the voltage across the

known resistance $R_{ref} = 1000$ Ohms. Figure 16 shows the circuit schematic for the RTD.

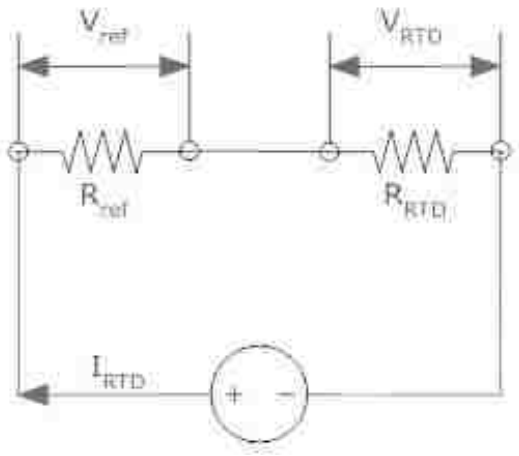

Figure 16: Electrical schematic for measuring the resistance across the RTD.

Volume flow rate in line (1) was measured by an FTO Series turbine flow meter by Flow Technology Inc. with an accuracy of 0.25% and a range of 3 – 303 mL/min. The differential pressure across each EHD pump was measured by two identical bi-directional differential pressure transducers by Omega Engineering Inc. The transducers had a range of -2500 to 2500 Pa and an accuracy of ±10 Pa. High D.C. voltage for the EHD pumps was supplied by two Glassman High Voltage MJ Series power supplies rated at 20 kV and 700 μA. The Glassman power supplies included voltage and current monitors used to record input voltage and current. The mass flow rate in line (3) was measured by a Rheotherm thermal flow meter by Intek Inc. This particular flow meter was chosen because its flow-through design imposed a relatively low pressure drop on line (3) and allowed for a greater range of flow rates in that line during flow distribution tests. The flow meter accuracy is 2%, and its range is 0 – 500 g/min. However, this flow meter gave

readings which deviated from the factory calibration, and a field recalibration was recommended. The flow meter was recalibrated to the turbine flow meter in line (1), using a curve-fit to 13 points (13 degrees of freedom), and the resulting equation relating the voltage output to the mass flow rate had a standard error estimate of 6.9812 g/min. The reservoir of the system was a custom design made by stereolythography (SLA), and the polymer material used is an ABS-like plastic, Acurra 55, by 3D Systems Inc.

3.2. EHD Pump Design

The EHD pumps are the flush electrode type similar in design to that used by Pearson and Seyed-Yagoobi [25]. This type of design is not only easier to manufacture on small scales than the penetrating electrode design, but it is also more resistant to the intense vibration and accelerations seen by spacecraft at launch. In this design, electrodes in the form of discs are machined from stainless steel, and the electrical insulators, which separate the electrodes, are machined from polycarbonate. The triangular flow path in Figure 8 is machined into the discs, which are then stacked along copper electrical bus lines to form a flow passage through the center of the stack. A model of several electrode pairs is shown in Figure 17 along with the thicknesses of each layer. Notice that the high voltage (HV) electrodes intersect only the HV bus line, and the ground electrodes intersect only the grounded bus line. Firm electrical contact between the electrodes and bus lines is ensured by application of a conductive epoxy, Masterbond EP21TDC/SLO. Figure 18 is a photo of a fully assembled stack of 15 pairs of electrodes. Between each electrode pair is a layer of polycarbonate whose thickness is optimized to prevent interaction of the electric fields of adjacent pairs but minimize the length of the stack. The thicknesses of each electrode and insulator were chosen with guidance by a

theoretical study by Yazdani and Seyed-Yagoobi [27]. On each end of the stack, a 2" long section made by SLA provides a smooth transition from circular to triangular flow cross-sections. Each stainless steel electrode was de-burred and electro-polished to remove sharp edges that may cause excessive electric field concentrations and ion injection.

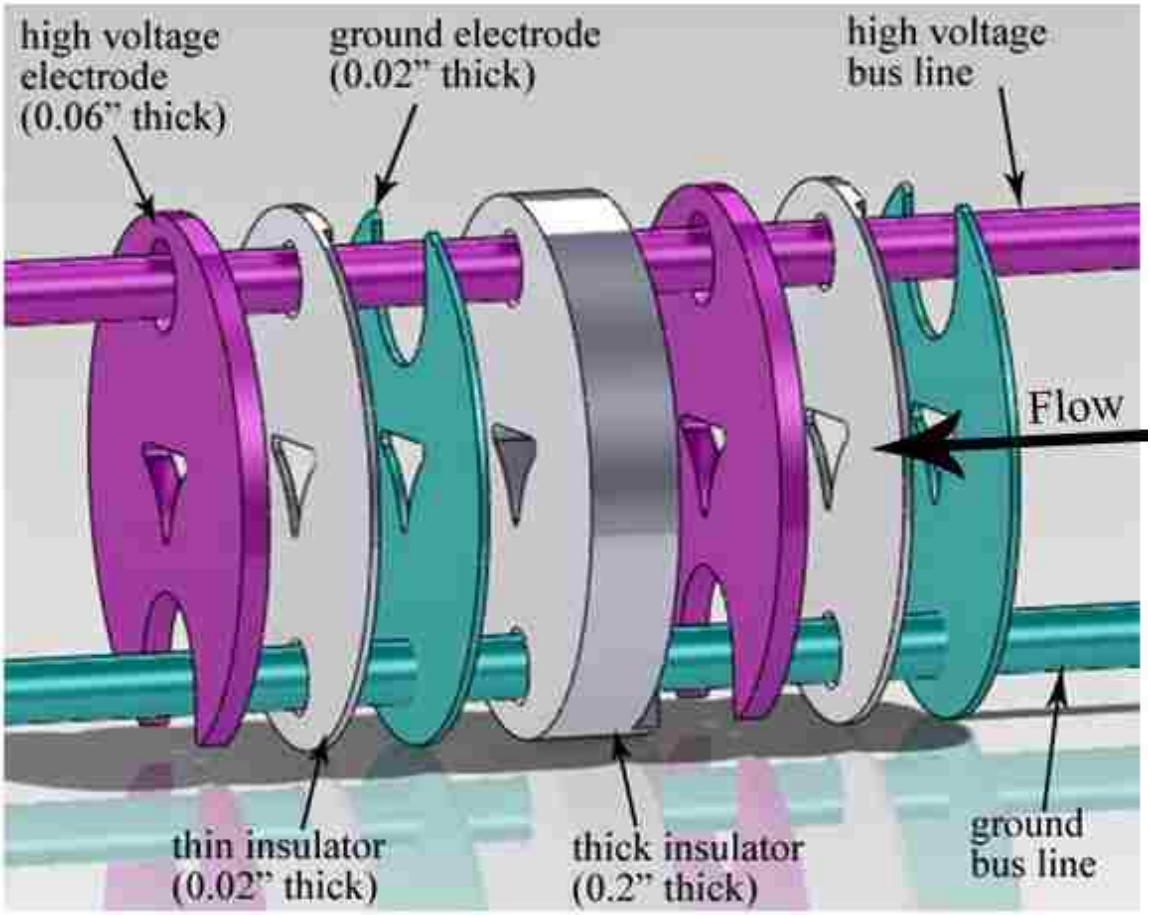

Figure 17: Three pairs of electrodes and insulating layers stacked along copper bus lines, showing thicknesses

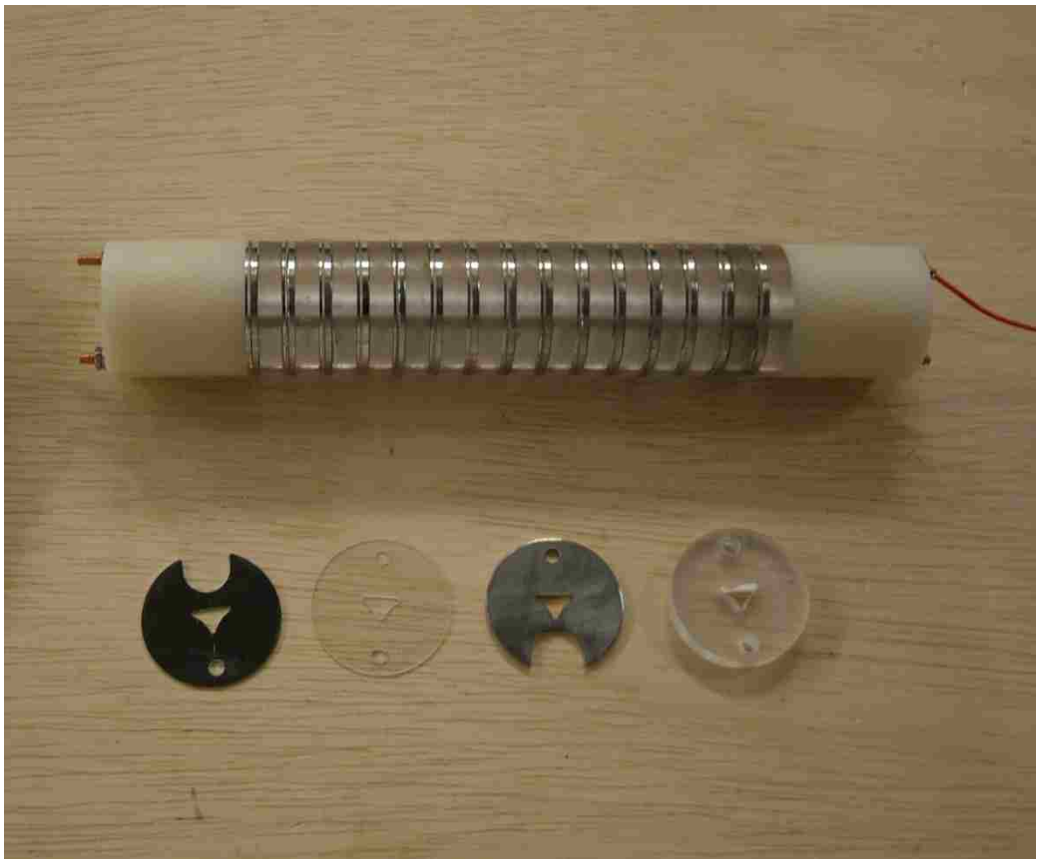

Figure 18: Photo of an assembled electrode stack with stainless steel electrodes and polycarbonate insulators.

The remainder of the pump structure is shown in Figure 19. The stack of electrodes is inserted into a snug-fitting polycarbonate tube, and the assembly is encapsulated by steel pipe. Threaded polycarbonate caps on the ends of the pipe provide a hermetic seal and connections to fluid lines. A safe high voltage (SHV) bulkhead connector feeds the high voltage bus line, and the grounded bus line is connected directly to the steel pipe. Before assembly, each piece of the EHD pump was soaked overnight and rinsed with alcohol to remove any debris. The interfaces between the polycarbonate

caps and the electrode stacks were designed such that fluid would naturally leak into the spaces surrounding the electrode stack. To ensure that all spaces within the pumps were filled with fluid, a vacuum pump was used to evacuate all air before fluid was allowed to enter.

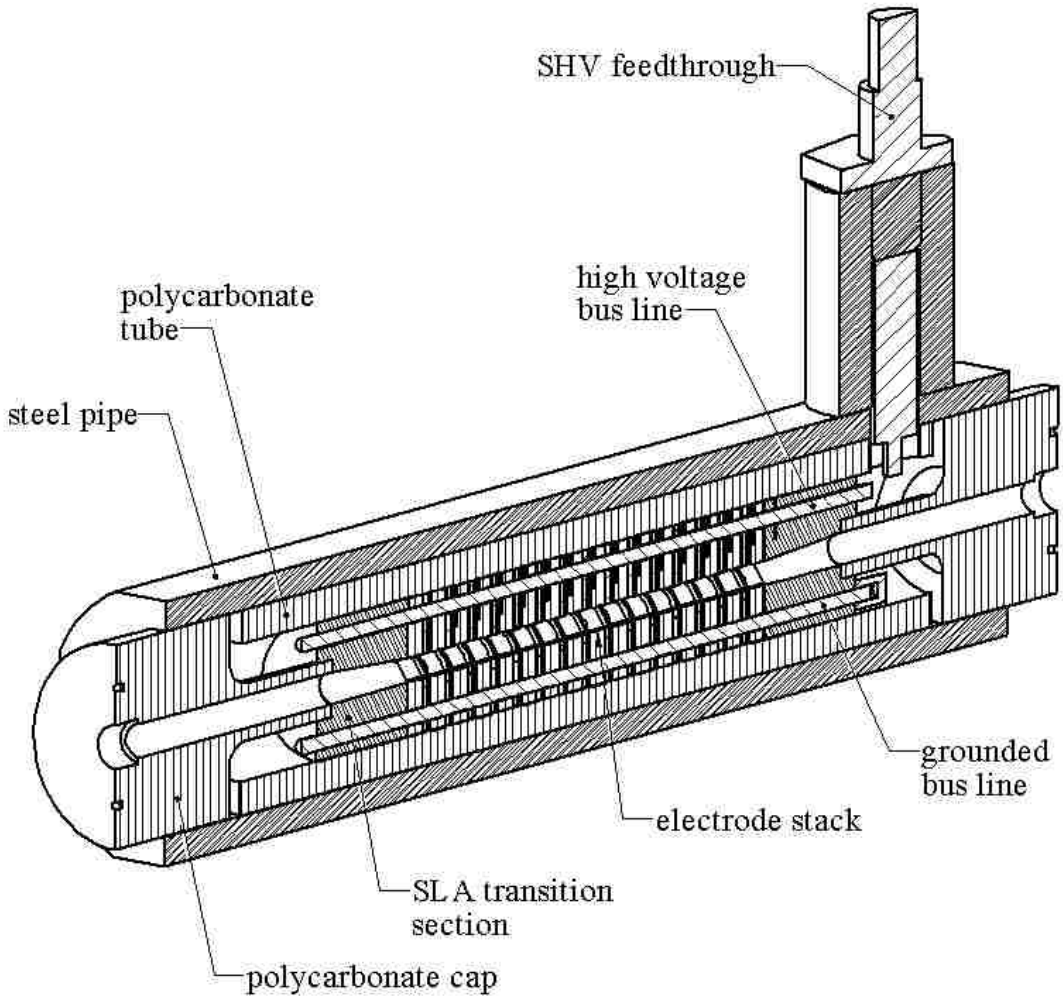

Figure 19: Internal structure of the EHD pumps.

3.3. Test Procedure

After the system was fully assembled and filled with fluid, the EHD pumps were activated for a short period to verify that there were no short circuits, and all instruments were checked for proper operation. The system was then disassembled and all components drained of fluid to remove any contaminants within the system. Formal testing was begun after the system was primed with fresh fluid.

Five types of tests were performed to characterize the performance of the two EHD pumps under various flow conditions: static tests, forward and reverse flow tests, and flow distribution tests representing configurations A and B from Figure 12. As shown in section 4.1, a process of conditioning the EHD pump interactions with the fluid can change the results of a given test. The application of a voltage sufficiently strong to induce flow (> 1 kV) coupled with flow through the EHD pumps increased the performance of the EHD pumps significantly for a period of time. Both the voltage and the flow must be non-zero for the conditioning to affect subsequent performance. This flow conditioning process was performed before every test with the exception of the static benchmark tests and consisted of setting the gear pump to produce 200 mL/min and setting the EHD pump to 2 kV for 1 hour. The duration of one hour was selected based on the amount of time the pumps needed to reach steady-state operation (shown in section 4.1), but no tests were performed to determine the proper flow rate or voltage settings for the conditioning process. Rather, these were a matter of judgment. Applied voltages in all tests did not exceed 3500 volts in order to avoid electrical breakdown of the fluid and arcing observed at higher voltages.

3.3.1. Static Tests

Static tests characterized the EHD pump performance in the absence of flow. The first type of static test is the benchmark test, which was performed with both pumps (a) and (b). In this type of test, the gear pump was idled, and the valves on either side of the EHD pumps were closed to prevent flow through the EHD pumps. The voltage was then set to 2 kV for approximately one hour and the pressure generation and current consumption were recorded. As shown in section 4.1, pump performance varied significantly from day to day, and benchmark tests were used to track those changes. Some benchmark tests were modified to include a flow conditioning process which consisted of leaving the EHD pump at 2 kV and stepping through flow rates from 0 to 300 mL/min. These extended benchmark tests showed the effects of flow conditioning on pump performance. Results for this test are shown in section 4.1. The second type of static test measured the static pressure generation and current consumption of the EHD pump at voltages ranging from 0 to 3500 volts. This was not performed as a separate test, but was built in to the forward and reverse flow tests discussed in the next section. The results for this test are given in section 4.2.

3.3.2. Forward and Reverse Flow Tests

Referring to objective #1 in section 2.2, the purpose of forward and reverse flow tests was to determine the effects of flow velocity on pump performance. These two types of tests are identical except for the direction in which the EHD pumps act relative to the flow velocity. In the forward flow tests, the pumping direction is the same as the flow velocity, and in the reverse tests, the pumping direction is opposite to that of the flow velocity. Figure 20 shows the paths of fluid flow in blue and the system configurations

for both types of tests. In forward flow, line (2) is closed, and flow is routed through line (3). In reverse flow, line (3) is closed, and flow is routed through line (2). Remember that only EHD pump (a) is active in these tests, while EHD pump (b) is idled.

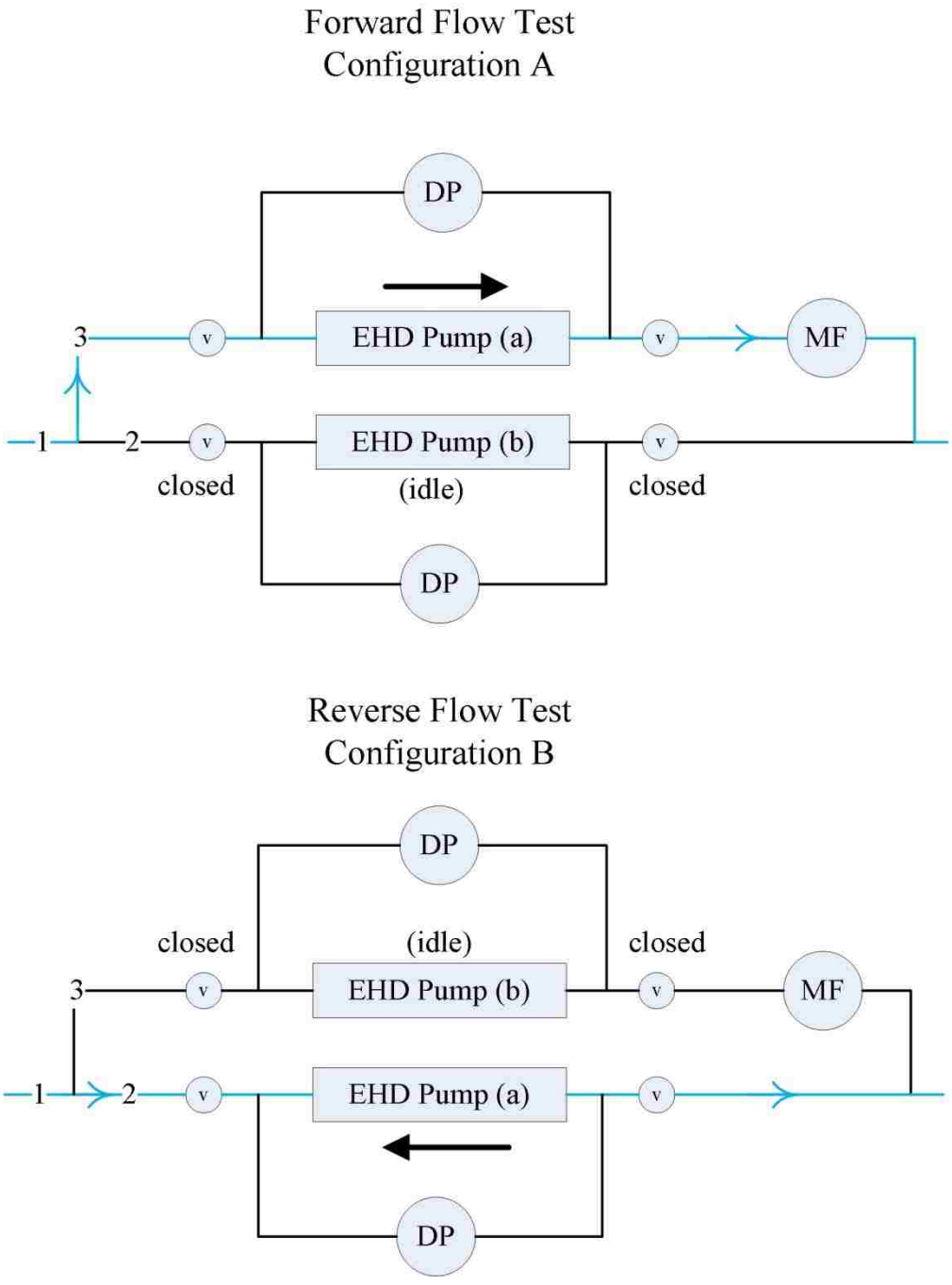

Figure 20: Flow paths for the forward (top) and reverse (bottom) flow tests.

In both tests, the EHD pump was set to a specified voltage and various flow rates were set by the gear pump. The next voltage was then set, and the system was cycled through the same flow rates again. Voltages were stepped up from 0.5 to 3.5 kV in increments of 0.5 kV, and flow rates were stepped up from 0 to 300 mL/min (0 to 20 cm/s velocity) in increments of 25 and 50 mL/min. This test procedure was always preceded by a conditioning period of one hour where voltage is 2 kV, and flow rate is 200 mL/min. Differential pressure across the EHD pump and current consumption are recorded. For each applied voltage, a flow rate versus differential pressure relationship is presented in the results section. The differential pressure reading has a component due to friction (always negative) and a component due to EHD effects. The component due to friction was measured separately and subtracted from the reading to obtain the differential pressure due to EHD effects only. Results for these tests are given in sections 4.3 and 4.4. Set points where the flow rate is zero show the static pressure generation and current consumption of the EHD pump and are used as data points to construct voltage-pressure and voltage-current characteristics for the pump.

3.3.3. Configuration A and B Distribution Tests

Referring to objective #2 in section 2.2, the purpose of the flow distribution tests was to characterize the capabilities of pumping configurations A and B from Figure 12 to modify an existing flow distribution between lines (2) and (3), and to demonstrate that the EHD pump can reroute flow through line (3) by imposing a pressure drop on line (2). These two types of tests were identical except for the system configuration. In configuration A, the active pump (pump (a)) was in line (3) pumping in the same direction as the flow velocity. In configuration B, the active pump was in line (2),

pumping in the direction opposite to flow velocity. Both system configurations are repeated here for convenience. Remember that only EHD pump (a) was active in these tests, while EHD pump (b) was idled.

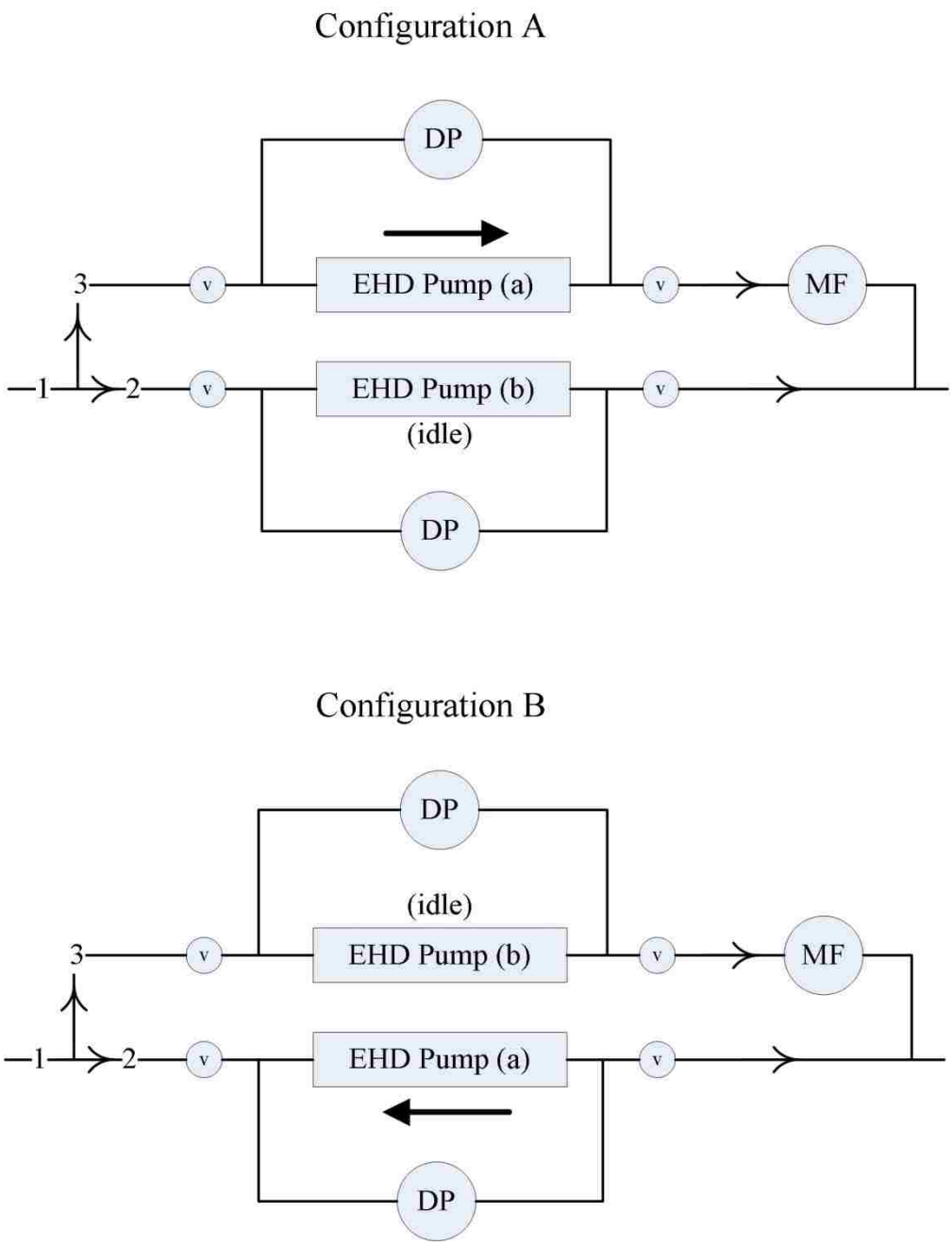

Figure 21: System configuration A (top) and configuration B (bottom).

In both tests, the gear pump was set to output a specified flow rate, and various voltages were applied to the EHD pump. The next flow rate was then set and the EHD pump was cycled through the same voltages again. Voltages were stepped up from 0.5 to 3.5 kV, and flow rates are stepped up from 0 to 300 mL/min (0 to 20 cm/s velocity). This test procedure was always preceded by a conditioning period of one hour where voltage is 2 kV and flow rate was 200 mL/min. As the voltage in the EHD pump was increased, the distribution of flow in lines (2) and (3) changed. Differential pressure across the EHD pump and current consumed by the pump are recorded. The performances of each configuration were compared by comparing the pump input power required to obtain a given flow rate in line (3). In configuration B, the active EHD pump is opposing an oncoming flow and may be considered a variable-resistance valve used to reroute flow to line (3). Results for these tests are given in sections 4.5 and 4.6.

3.4. Uncertainty Analysis

Uncertainties are reported according to the ASME standard of Abernathy, Benedict, and Dowdell [37]. Measurement error has a random component (precision error) and a fixed component (bias error). Precision error is quantified by taking N samples from the parent population and calculating the precision index of the sample population

$$S_X = \left[\frac{1}{N-1}\sum_{i=1}^{N}(X_i - \bar{X})^2\right]^{1/2} \tag{3.5}$$

where X_i are the values of the samples and $\bar{X}$ is the mean of the sample population. If one were to take the average of M readings from the sample population, then the precision

index for that average value, $S_{\bar{X}}$, is reduced relative to the precision index of the sample population according to

$$S_{\bar{X}} = \frac{S_X}{\sqrt{M}} \tag{3.6}$$

Bias error is not known for a given measurement and must be estimated. Bias error comes from many sources which are grouped into the categories of calibration, data acquisition, and data reduction. The uncertainties given by manufactures of measurement instrumentation are taken as limits to the calibration bias, B_1, and likewise, the uncertainty with which the data acquisition unit measures outputs from the instruments is taken as the limit to data acquisition bias, B_2. These bias limits are variable but have a known relationship to the value of the measurement, so that bias values for multiple samples of a given measurement should be equal. Bias due to data reduction, B_3, comes from inaccuracies in curve-fitting and is the Standard Error Estimation (SEE) of the curve-fit [38]. These sources of bias error are combined into one number, B, using the root sum square method (RSS)

$$B = \left({B_1}^2 + {B_2}^2 + {B_3}^2\right)^{1/2} \tag{3.7}$$

An uncertainty interval, U, for a given parameter is then calculated by combining the precision and bias limits according to

$$U = [B^2 + (tS_X)^2]^{1/2} \tag{3.8}$$

where the Student t value is a function of the number of samples *N* or *M* (commonly referred to as degrees of freedom) used in calculating S_X or $S_{\bar{X}}$. The quantity tS_X is called

the precision limit. This method produces U with a confidence level of 95%, that is, the odds are 19:1 that the true value of the measured parameter lies within the interval of $X_i \pm U$ or $\bar{X} \pm U$. The uncertainty of a given parameter is propagated into any result which relies on that measurement. For a result, r, that is a function of multiple parameters, g_w

$$r = f(g_1, g_2, \ldots g_w) \tag{3.9}$$

the law of propagation of uncertainty by Kline and McClintock [39] is used. The precision index and bias limit of the result, S_r and B_r respectively, are calculated first and combined into an uncertainty interval, U_r, in the last step of the process

$$S_r = \left[\sum_{i=1}^{J} \frac{dr}{dp_i} S_i\right]^{1/2} \tag{3.10}$$

$$B_r = \left[\sum_{i=1}^{J} \frac{dr}{dp_i} B_i\right]^{1/2} \tag{3.11}$$

$$U_r = \left[{B_r}^2 + (tS_r)^2\right]^{1/2} \tag{3.12}$$

where again *t* is a function of the degrees of freedom. If one were to take the average of value of a result, *r*, from *M* tests, the bias limit of that average result would be equal to the bias limit of the result from a single test, and the precision index of that average result, $S_{\bar{r}}$, would be reduced from that of a single test according to

$$S_{\bar{r}} = \frac{S_r}{\sqrt{M}} \tag{3.13}$$

where the precision index of the population of test results is

$$S_r = \left[\frac{1}{N-1}\sum_{i=1}^{N}(r_i - \bar{r})^2\right]^{1/2} \tag{3.14}$$

For a single test, each data point reported was the average of 64 readings. By equation (3.6), the precision limit was very small and was often much smaller than the bias limit. The contribution to the bias limit due to the data acquisition unit was also very small. Consequently, bias due to calibration of the instruments and due to curve fitting tended to dominate uncertainty in a given measurement. For each parameter that was measured, Table 3 gives the typical range of values seen during testing, the maximum values for the bias limits seen in testing, and the maximum percent of reading seen in testing. To show the effects of uncertainty propagation to results, sample uncertainties from a configuration A flow distribution test are given in Table 4.

The equations for bias and precision limits for results are given in the following sections. Because equations for precision limits are identical to those of the bias limits for all results except fluid temperature, mass flow rate in line (3), and differential pressure due to friction, precision limit equations are included only for those three results. Bias and precision limits for a given result, such as flow velocity through the EHD pump, will vary depending on the configuration of the system. One equation that is valid for both configurations is given, and any differences brought by changing configurations are noted in the text.

As shown in the results sections, results from a single test repeated over many days varied considerably. In those sections, what is reported is the average of results from several days, but to capture the day-to-day variability, precision indexes from the

population of test results, equation (3.14), are used in plotting the uncertainties, instead of the precision index of the average of the test results, equation (3.13).

Table 3: Typical range of values seen during testing, the maximum values for the bias limits seen in testing, and the maximum percent of reading seen in testing

Measurement	Units	Typical Measurement Range	Max Absolute Bias Limit	Maximum % of Reading
Applied Voltage	V	500 – 3500	72.9	4.5
Applied Current	μA	0 - 70	0.85	5.5
Total Flow	mL/min	3.84 - 300	0.75	0.25
Line (3) Flow	g/min	0 - 500	11.2	
Absolute Pressure	kPa	85 - 101	1.4	1.75
Differential Pressure	Pa	-2000 - 2000	10	
Fluid Temperature	°C	18 - 25	0.21	1.4

Table 4: Sample uncertainty calculations (Flow Distribution Test configuration A)

Parameter	Units	Reference Value	Absolute Uncertainty	Relative Uncertainty (%)
Applied Voltage	V	2499	61	2.4
Applied Current	μA	13.6	0.53	3.9
Total Flow	mL/min	149.5	0.67	0.4
Line (2) Flow	mL/min	94.0	5.3	5.6
Line (3) Flow	g/min	85.8	8.1	9.4
Line (3) Flow	mL/min	55.6	5.2	9.4
Absolute Pressure	kPa	91.2	1.4	1.5
Differential Pressure Reading	Pa	201.8	10.4	5.1
Pressure Drop due to Friction	Pa	-43.7	7.8	17.8
Pressure due to EHD Effects	Pa	245.5	13.0	5.3
Fluid Temperature	°C	22	0.24	1.11
Fluid Density	kg/m^3	1545	0.43	0.028
Velocity through EHD Pump	cm/s	3.8	0.0003	0.0075
Re through EHD Pump		87	0.4	0.5

3.4.1. Bias of Data Acquisition Unit

The bias for a voltage measurement B_V by the Omega Personal DAQ-56 data acquisition unit is

$$B_V = (0.00002)RG + (0.0001)RD \tag{3.15}$$

where RG is the voltage range the channel is set to measure, and RD is the voltage reading in volts.

3.4.2. Bias and Precision Limits of Fluid Temperature

The bias limit of fluid temperature, B_T, must be calculated in several steps. It is a result of the bias limits of the current put through the RTD, $B_{I_{RTD}}$, the bias limit of the resistance of the RTD, $B_{R_{RTD}}$, the bias limit caused by calibration of the RTD, B_{T2}, and the bias limits of the data acquisition unit. The current through the RTD, I_{RTD}, is calculated from the voltage drop, V_{ref}, across a known resistance, R_{ref}

$$I_{RTD} = \frac{V_{ref}}{R_{ref}} \tag{3.16}$$

and the bias limit for I_{RTD} is

$$B_{I_{RTD}} = \sqrt{\left(\frac{1}{R_{ref}} B_{V_{ref}}\right)^2 + \left(\frac{V_{ref}}{{R_{ref}}^2} B_{R_{ref}}\right)^2} \tag{3.17}$$

Next, the resistance of the RTD, R_{RTD}, is calculated from the voltage drop across the RTD, V_{RTD}, for a known current, I_{RTD}

$$R_{RTD} = \frac{V_{RTD}}{I_{RTD}} \tag{3.18}$$

and the bias limit for this resistance is

$$B_{R_{RTD}} = \sqrt{\left(\frac{1}{I_{RTD}} B_{V_{RTD}}\right)^2 + \left(\frac{V_{RTD}}{{I_{RTD}}^2} B_{I_{RTD}}\right)^2} \tag{3.19}$$

The temperature can then be calculated according to the relationship

$$T = \frac{R_{RTD} - 100}{0.385} \tag{3.20}$$

and the bias of the temperature, B_{T1}, due to $B_{R_{RTD}}$ is

$$B_{T1} = \frac{1}{0.385} B_{R_{RTD}} \tag{3.21}$$

The bias limit due to the calibration is

$$B_{T2} = (0.002)T + 0.15 \tag{3.22}$$

B_{T1} and B_{T2} are combined by RSS to give the total bias limit of the fluid temperature

$$B_T = \sqrt{{B_{T1}}^2 + {B_{T2}}^2} \tag{3.23}$$

$B_{V_{ref}}$ and $B_{V_{RTD}}$ are biases due to the data the acquisition unit and are calculated according to equation (3.15). Table 5 lists the variables used in the above calculations.

The precision limit for temperature is calculated in a similar manner, but the process is simpler because the resistor does not contribute to precision errors. The precision limits of the reference voltage and the voltage drop across the RTD, $S_{V_{ref}}$ and $S_{V_{RTD}}$ respectively, are known and used with the following equations to calculate the precision limit of the fluid temperature

$$S_{I_{RTD}} = \frac{S_{V_{ref}}}{R_{ref}} \tag{3.24}$$

$$S_{R_{RTD}} = \sqrt{\left(\frac{1}{I_{RTD}} S_{V_{RTD}}\right)^2 + \left(\frac{V_{RTD}}{{I_{RTD}}^2} S_{I_{RTD}}\right)^2} \tag{3.25}$$

$$S_T = \frac{1}{0.385} S_{R_{RTD}} \tag{3.26}$$

Table 6 lists the variables used in these precision calculations.

Table 5: Variables used in bias calculations for fluid temperature

T	Fluid temperature
I_{RTD}	Current through the RTD
$B_{I_{RTD}}$	Bias of current through RTD
R_{ref}	Reference resistance
$B_{R_{ref}}$	Tolerance of reference resistance
V_{ref}	Voltage drop across the reference resistor
$B_{V_{ref}}$	Bias of reference voltage due to data acquisition unit
$B_{R_{RTD}}$	Bias of RTD Resistance
V_{RTD}	Voltage drop across RTD
$B_{V_{RTD}}$	Bias of voltage drop across RTD due to data acquisition unit
B_{T1}	Bias of fluid temperature due to $B_{R_{RTD}}$
B_{T2}	Calibration bias given by manufacturer
B_T	Total bias of fluid temperature

Table 6: Variables used in precision calculations for fluid temperature

$S_{I_{RTD}}$	Precision of the current through the RTD
$S_{V_{ref}}$	Precision of the voltage drop across the reference resistor
$S_{R_{RTD}}$	Precision of the RTD resistance
S_T	Precision of the fluid temperature

3.4.3. Bias Limit of Fluid Density

The density ρ is calculated directly from the fluid temperature using the equation provided by the fluid manufacturer (3M)

$$\rho = -1.755(T) + 1583.8 \tag{3.27}$$

and the bias limit of the density is a simple scaling of the bias limit of temperature

$$B_\rho = (1.755)B_T \tag{3.28}$$

3.4.4. Bias Limit of Fluid Dynamic Viscosity

Fluid dynamic viscosity, μ, is a function of density and temperature according to the equation provided by the fluid manufacturer, 3M

$$\mu = \rho(1E-6)\left\{exp\left(\frac{464.403382}{T+133} - 2.881482\right)\right\} \tag{3.29}$$

and the bias limit of dynamic viscosity is

$$B_\mu = \sqrt{\left(\frac{d\mu}{d\rho}B_\rho\right)^2 + \left(\frac{d\mu}{dT}B_T\right)^2} \tag{3.30}$$

$$\frac{d\mu}{d\rho} = (1E-6)\left\{exp\left(\frac{464.403382}{T+133} - 2.881482\right)\right\} \tag{3.31}$$

$$\frac{d\mu}{dT} = \rho(2.60306E-5)\left\{\frac{\exp\left(\frac{464.403382}{T+133}\right)}{(T+133)^2}\right\} \tag{3.32}$$

3.4.5. Bias and Precision Limits of Mass Flow Rate in Line (3)

The bias limit of the mass flow measurement in line (3) is a result of the calibration bias limit provided by the manufacturer (Intek Inc.) for current output of the

flow meter, $B_{I_{intek}}$, the bias limit of the voltage drop across the resistor, $B_{V_{intek}}$, and the curve fit for the recalibration of the flow meter, $B_{Q_{3g}2}$. The flow meter is calibrated to output a current, I_{intek}, with a bias limit, $B_{I_{intek}}$, of 2%, or

$$B_{I_{intek}} = (0.02)I_{intek} \tag{3.33}$$

Current is not measured directly, but the voltage drop, V_{intek} , across a known resistance, R_{intek}, due to I_{intek} is measured, and its bias limit is

$$B_{V_{intek}1} = \sqrt{\left(R_{intek}B_{I_{intek}}\right)^2 + \left(I_{intek}B_{R_{intek}}\right)^2} \tag{3.34}$$

where $B_{R_{intek}}$ is the tolerance of the resistor. This bias limit of the voltage is combined with the bias limit due to the data acquisition unit, $B_{V_{intek}\,2}$, that is calculated according to equation (3.15)

$$B_{V_{intek}} = \sqrt{{B_{V_{intek}1}}^2 + {B_{V_{intek}\,2}}^2} \tag{3.35}$$

The mass flow rate, Q_{3g}, is calculated according to the curve-fit relationship to V_{intek}

$$Q_{3g} = (116.72)V_{intek} - 116.06 \tag{3.36}$$

and the bias in mass flow rate scales with bias of the voltage

$$B_{Q_{3g}1} = (116.62)B_{V_{intek}} \tag{3.37}$$

The standard error estimate of this curve fit (6.9812 g/min) is combined by RSS with $B_{Q_{3g}1}$ to yield the total bias limit for the mass flow rate in line (3)

$$B_{Q_{3g}} = \sqrt{{B_{Q_{3g}1}}^2 + 6.9812^2} \tag{3.38}$$

Table 7 lists the variables used in the above calculations. The precision limit of voltage output of the mass flow meter, $S_{V_{intek}}$, is known and the precision of the mass flow measurement is

$$S_{Q_{3g}} = (116.72)S_{V_{intek}} \tag{3.39}$$

Table 7: Variables used in bias calculations for mass flow rate in line (3)

Q_{3g}	Mass flow rate in line (3)
I_{intek}	Current output of the mass flow meter
$B_{I_{intek}}$	Bias limit of the current output
V_{intek}	Voltage reading converted from current output
$B_{V_{intek}1}$	Bias of voltage reading propagated from current output
$B_{V_{intek}2}$	Bias of voltage reading due to data acquisition unit
$B_{V_{intek}}$	Total bias of voltage reading
R_{intek}	Resistance to convert current to voltage
$B_{R_{intek}}$	Tolerance of R_{intek}
$B_{Q_{3g}1}$	Bias of mass flow rate due to $B_{V_{intek}}$
$B_{Q_{3g}2}$	Standard error estimate of curve-fit (6.9812 g/min)
$B_{Q_{3g}}$	Total Bias of mass flow rate
$B_{Q_{3g}}$	Total bias of fluid temperature

3.4.6. Bias Limit of Volume Flow Rate in Line (3)

The volume flow rate in line (3) in mL/min, Q_{3mL}, is calculated by dividing the mass flow rate by the density

$$Q_{3mL} = 1000\frac{Q_{3g}}{\rho} \tag{3.40}$$

where the density in kg/m^3 and the mass flow rate, Q_{3g}, is in g/min. The bias limit of the volume flow rate in line (3) is

$$B_{Q_{3mL}} = \sqrt{\left(\frac{1000}{\rho} B_{Q_{3g}}\right)^2 + \left(1000 \frac{Q_{3g}}{\rho^2} B_\rho\right)^2} \tag{3.41}$$

3.4.7. Bias Limit of Volume Flow Rate in Line (2)

The volumetric flow rate in line (2) in mL/min, Q_{2mL}, is calculated by subtracting the flow rate in line (3) from the total flow rate

$$Q_{2mL} = Q_{total\,mL} - Q_{3mL} \tag{3.42}$$

and the bias limits of the total flow rate and the flow rate in line (3) propagate to yield the bias limit of the flow rate in line (2)

$$B_{Q_{2mL}} = \sqrt{\left(B_{Q_{total\,mL}}\right)^2 + \left(B_{Q_{3mL}}\right)^2} \tag{3.43}$$

3.4.8. Bias Limit of Flow Velocity through EHD Pump

The flow velocity through the EHD pump is

$$v = \frac{Q}{24.79e-6} \tag{3.44}$$

where v is the flow velocity in m/s, Q is the volume flow rate in m^3/s, and the area of the flow cross-section of the EHD pump is 24.79E-6 m^2. The bias and precision limits of the flow velocity through the EHD pump scale with area of the flow cross-section of the pump

$$B_v = \frac{B_Q}{24.79e-6} \tag{3.45}$$

Flow rate through line (3) is used for configuration A and flow rate through line (2) is used for configuration B.

3.4.9. Bias and Precision Limits of Differential Pressure across EHD Pump Due to Friction

The differential pressure across the EHD pump due to friction, dP_f, is dependent on the volume flow rate through the EHD pump, and calculated from a curve fit relationship

$$dP_f = -(0.0025)Q^2 - (0.5161)Q - 5.97 \tag{3.46}$$

The bias for this differential pressure is the RSS of the bias of flow rate, Q, and the Standard Error Estimate of the curve fit (6.9868 Pa)

$$B_{dP_f} = \sqrt{\left(B_{dP_f}\right)^2 + 6.9868^2} \tag{3.47}$$

Where

$$B_{dP_f} = [-2(0.0025)Q - (0.5161)]B_Q \tag{3.48}$$

The corresponding precision limit is

$$S_{dP_f} = [-2(0.0025)Q - (0.5161)]S_Q \tag{3.49}$$

The flow rates through lines (3) and (2) are used for configurations A and B, respectively.

3.4.10. Bias Limit of Differential Pressure across EHD Pump Due to EHD Effects

The bias limit of the differential pressure across the EHD pump due to EHD effects only, dP_{net}, is the difference between the differential pressure reading, dP, and the estimated pressure drop through the pump due to friction, dP_f

$$dP_{net} = dP - dP_f \tag{3.50}$$

and the bias limit is

$$B_{dP_{net}} = \sqrt{(B_{dP})^2 + \left(B_{dP_f}\right)^2} \tag{3.51}$$

3.4.11. Bias Limit of EHD Pump Power Input

The electrical power input to the EHD pumps, φ_{in}, is the product of the applied voltage, e, and the current consumed by the pump, I

$$\varphi_{in} = eI \tag{3.52}$$

so that the bias limit of the power input is

$$B_{\varphi_{in}} = \sqrt{(IB_e)^2 + (eB_I)^2} \tag{3.53}$$

3.4.12. Bias and Precision Limits of Reynolds Number through EHD Pump

The Reynolds Number through the EHD pump is

$$Re = \frac{v\rho D_h}{\mu} \tag{3.54}$$

where the hydraulic diameter $D_h = 0.0025377$ m. The bias limit for Reynolds number is

$$B_{Re} = \left[\left(\frac{\rho D_h}{\mu} B_v\right)^2 + \left(\frac{v D_h}{\mu} B_\rho\right)^2 + \left(\frac{v \rho D_h}{\mu^2} B_\mu\right)^2\right]^{1/2} \tag{3.55}$$

Flow velocity and the bias limit of flow velocity are configuration dependent according to equations (3.44) and (3.45).

4. Results and Discussion

Results for the five types of tests are discussed in this section. Results for forward and reverse flow tests and for flow distribution tests are given as averages over several separate tests performed on separate days. Results usually varied significantly from day to day. To capture this variation in results, calculations of uncertainty use the precision indexes of the sample population (equation (3.14)) instead of the precision indexes of the average of the sample population (equation (3.13)).

4.1. Static Benchmark Test Results

Benchmark tests were performed for both EHD pumps; Figure 22 shows the results of a single test where both pumps are tested simultaneously. At the beginning of the test, the voltage across both pumps was set to 2 kV. Pressure generation and current consumption by each pump were recorded for one hour to determine the response of the stationary fluid to a sudden application of an electric field. Current is initially very high, but quickly decays to a steady-state value. This decay to steady-state is due to removal of ions present in the fluid before the field is applied and is refered to as “electrical purification” by Adamczewski [17]. The generated pressure spikes when the electric field is initially applied, then rises to a steady-state value.

This type of test was repeated on each day of testing as the first test performed each day, with no flow conditioning performed prior to activation of the pumps. Note that the results for the two pumps differed significantly because the uncertainty in pressure is only about ±10 Pa, and that in current is less than ±1 μA. Results for each pump also

differed from day to day. Neither the performances of the individual pumps nor their performance relative to one another followed any discernable pattern from day to day.

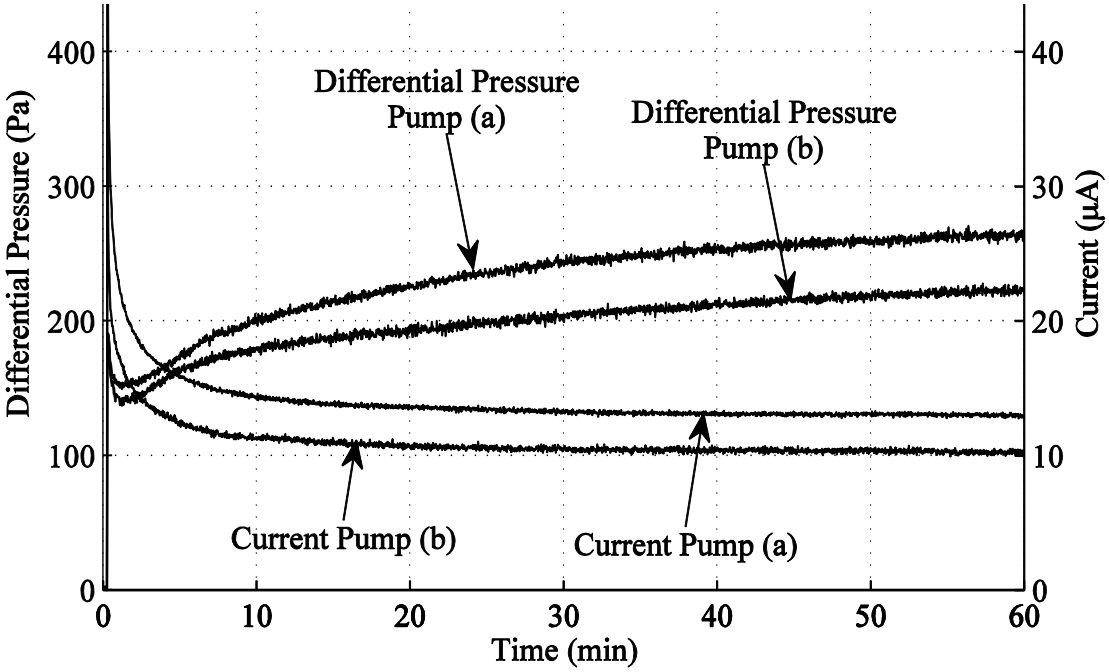

Figure 22: Sample benchmark test for pumps (a) and (b) showing the pressure and current responses to the sudden application of an electric field vs. time. Voltage setting is 2kV. Date: 1/19/2012

The differences in performance between pumps (a) and (b) may be caused by minute differences in construction or a malfunction of one of the pumps. Though the pumps are identical in design, and were fabricated and assembled by identical processes, small differences in electrode geometry or surface finish may produce different results. The difference in results should not be caused by differences in essential geometries such as thicknesses of the electrodes and insulators, since those thicknesses were set with a tolerance less than ±40 μm. The pressure generation and current consumption of pump

(b), which is consistantly lower than that of pump (a), may indicate the failure of electrical contact between an electrode and a bus line within pump (b). Though all electrical connections were checked after assembling the electrode stacks, it is possible that a connection was broken during the final stages of pump assembly or subsequently. Another possible cause for the difference in performance is the release of impurities into a volume of fluid within an EHD pump which does not mix with the flow through the center of the electrode stack. Several such areas are visible in Figure 19. Fluid trapped in areas around the electrode stack may have different properties than the fluid flowing through the center. Minimal electric conduction may take place in these areas, the magnitude of which may differ between the two pumps because of different fluid properties. Because subsequent testing required that the pump in different system configurations have similar performance characterisitics, pump (b) was excluded from testing, and system components were re-arranged to accomplish all tests using only pump (a). This reconfiguration was discussed in section 3.1.1.

Figure 23 shows the pressure and current for benchmark tests of pump (a) along with fluid temperatures on various dates ranging from October 20, 2011 to January 19, 2012. Each data point is an average over the final 5 minutes of each test. There appears to be no correlation between pump performance and fluid temperature that varied as much as 10 °C between tests.

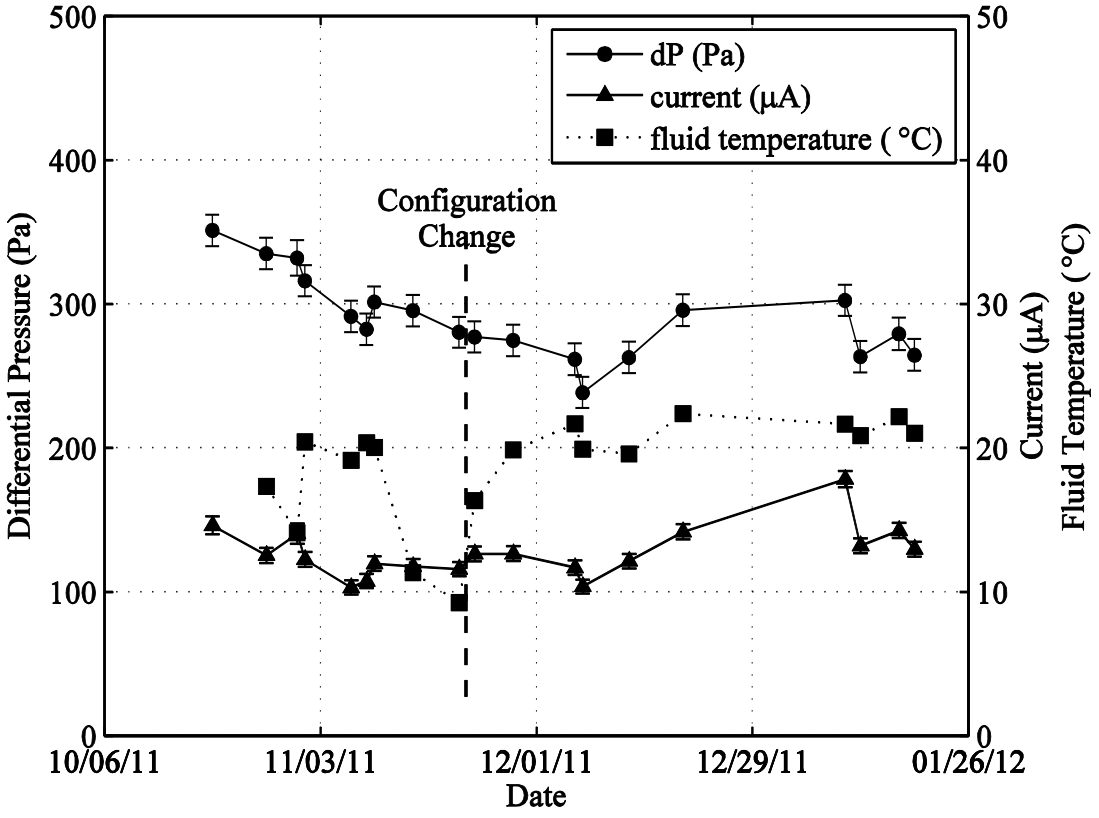

Figure 23: Pressure, current, and temperature results for benchmark tests on various dates using pump (a). Data points are averages over 5 minutes at the end of each test.

The large variation in day-to-day performance of pump (a) shown in Figure 23 may have several causes. The first is that some elements of the system may be incompatible with the working fluid. The Accura 55 plastic used in SLA parts and the conductive epoxy used to connect electrodes to the bus lines are both suspect. Conversations with the fluid manufacturer, 3M, and the epoxy manufacturer, Masterbond, indicated that neither the SLA plastic nor the conductive epoxy should

effect the electrical properties of Novec 7600, and a compatibility test showed that a sample of the Accura 55 gained only 0.04% mass after soaking in the fluid for 58 days. Nevertheless, no thorough investigation of the effects of these materials on the electrical properties of Novec 7600 was performed. In general, only materials which are approved by 3M for use with Novec 7600 were in contact with the fluid. Material incompatibility may contribute, but is not likely to be the only cause, as one would expect a monotonic increase or decrease in performance as the fluid leeches chemicals from incompatible materials. A second cause may be impurities entering the system through the atmosphere. The reservoir is open to the atmosphere through a breather filtered to 20 microns. Any particles, water vapor, or other substances which pass through the filter may be absorbed by the fluid and may cause undesired reactions when influenced by the strong electric fields used in EHD pumping. Impurities may also enter the system while it is being reconfigured, though there is no significant change in performance after a configuration change. The date when the system components were reconfigured is marked in Figure 23.

Benchmark tests performed after January 19, 2012 were modified to include a flow conditioning period that consisted of opening the valves around pump (a) and stepping through flowrates ranging from 0 to 300 mL/min. Figure 24 shows the pressure and current results for an input voltage of 2 kV. Differential pressure and current after the conditioning period (315 Pa, 11.4 μA) are significantly greater than before the conditioning period (227 Pa, 8.9 μA). Similar jumps in performance were present in every extended benchmark test, but the magnitudes varied from day to day. Figure 25 shows data from the original benchmark tests as well data prior to and after the conditioning period from the extended benchmark tests. Benchmark data collected prior

to implementing the flow conditioning period (shown in Figure 23) use the same symbols as the later data collected just before the conditioning period. Data before and after conditioning represent averages of the readings ever five minutes directly preceding and directly succeeding the flow conditioning period, respectively.

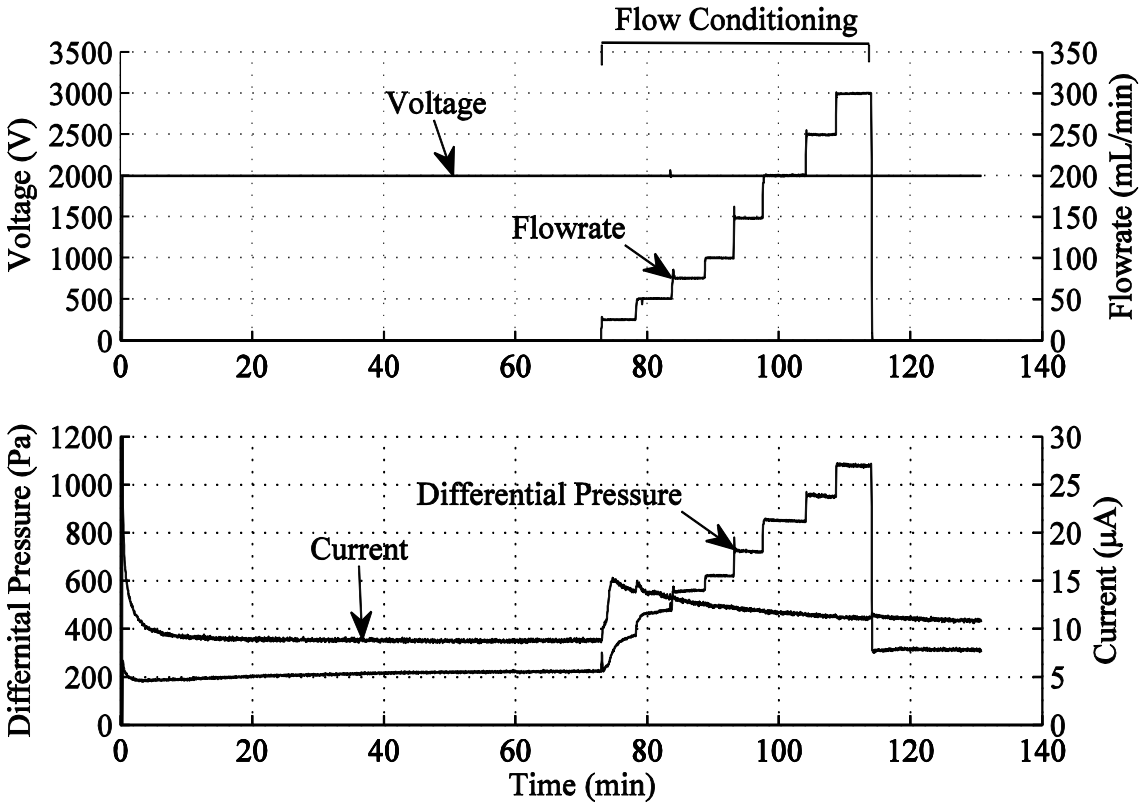

Figure 24: Sample extended benchmark test; voltage and flow rate inputs (top) and pressure and current results (bottom) vs. time. Date: 2/15/2012.

After the main body of testing was completed, the system was completely emptied of fluid and refilled with fresh fluid. Results for extended benchmark tests using new fluid are also shown in Figure 25. Generated pressure and current consumption using fresh fluid are significantly lower than when using fluid that had been used for several

months. This indicates that something in the system had been affecting the electrical properties of the fluid.

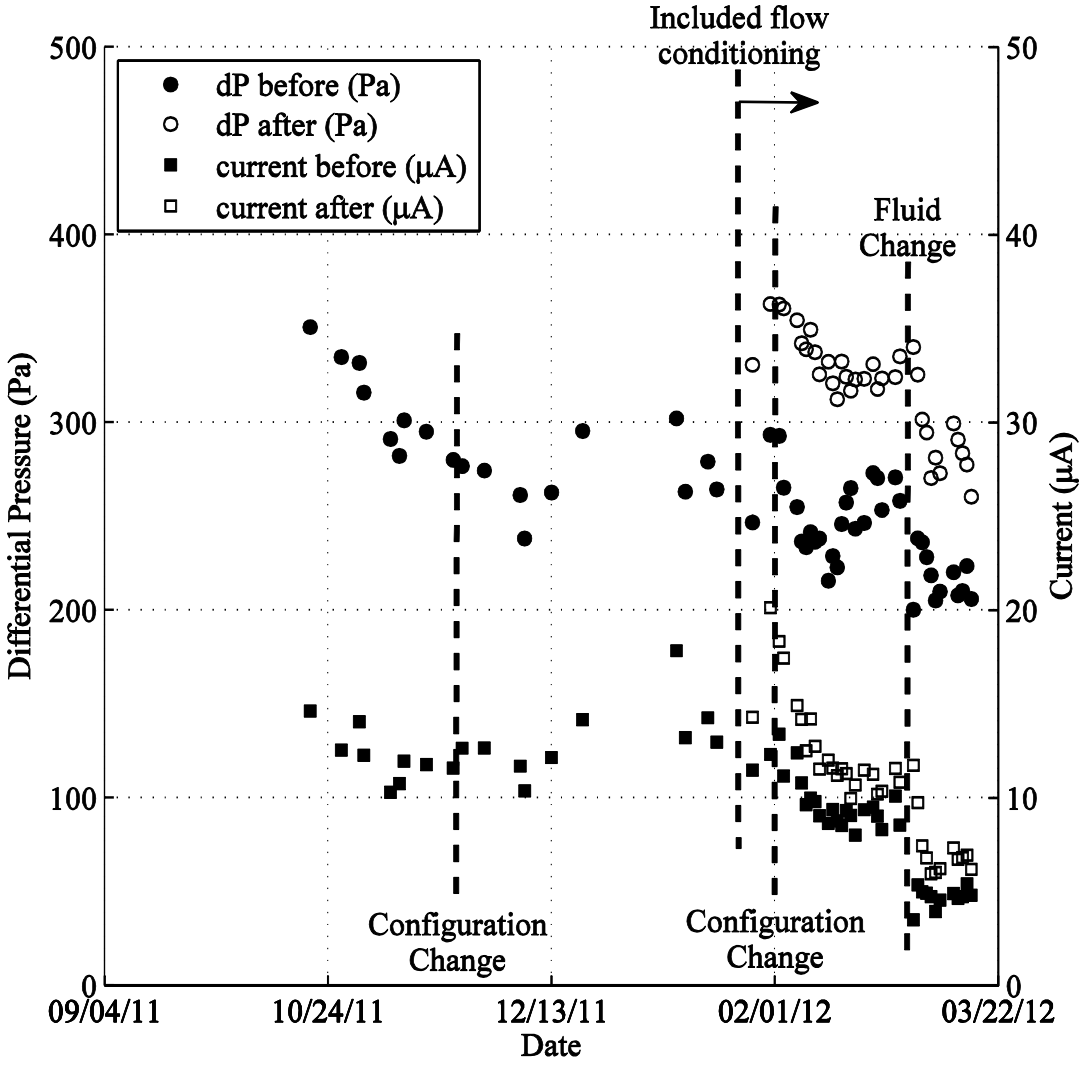

Figure 25: Pressure and current results from all benchmark tests, including data from before and after flow conditioning in extended benchmark tests. Average uncertainty in pressure = ±13.8 Pa, average uncertainty in current = ±0.47 µA.

4.2. Voltage-Pressure and Voltage-Current Characteristics

Data used to determine the voltage-pressure and voltage-current characteristics of pump (a) were taken from forward and reverse flow tests that are presented in the next section. Forward and reverse flow tests were not performed on pump (b), so no corresponding data are available for that pump. Results from set points at zero flow rate and at various voltages were extracted from fourteen forward and reverse flow tests and averaged. Data were included only from forward and reverse flow tests where preceding flows and voltages where high enough to condition the flow, so that they represent the static pressure generation and current consumption of a pump that has been active for some time. Figure 26 shows the characteristics of pump (a) for voltages ranging from 0 to 3500 volts, giving electric field strengths of 0 to 2.3 MV/m using an inter-electrode gap of 1.5 mm. Both pressure and current increase with the applied voltage. Though the pumps operate well into the intermediate field region described by Gallagher [16], the voltage-current characterisic for this fluid is linear, indicating that the non-linear voltage-current characteristic is not suitable for this fluid. Referring to the charge transport model in section 1.3.2, this linear increase in current must be due to an increase in the speed of charge migration ($b_i\vec{E}$ term in equation (1.8)) because the contribution to charge transport by diffusion is negligible, and there is no charge convection. Data in the plot are averages over many days of testing, but the uncertainty intervals shown do not use the precision index of the average results (equation (3.13)), but instead use the precision index of the entire sample poulation (equation (3.14)), so that they show the day-to-day variability of results.

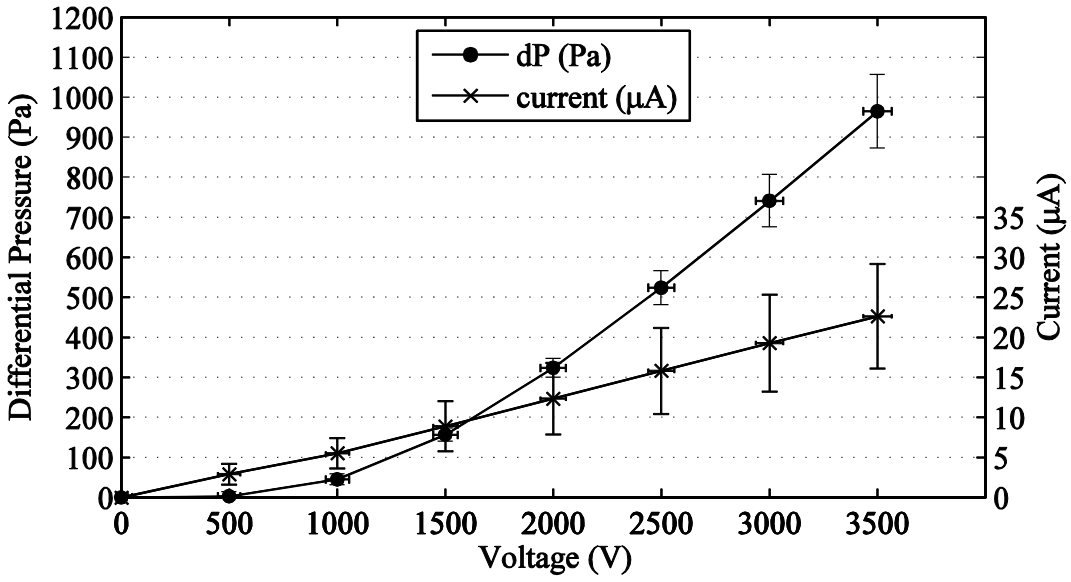

Figure 26: Voltage-pressure and voltage-current characteristics for EHD pump (a).

4.3. Forward Flow Test Results

Forward flow tests were used to determine the effects of flow velocity on pressure generation by and current consumption of the EHD pump. Figure 27 shows the direction of pumping forces and the direction of net flow for this type of test. Figure 28 shows voltage and flow rate settings (top) along with resulting readings for differential pressure, current, and fluid temperature (middle and bottom). Differential pressure is always measured as downstream minus upstream pressure. Voltage was set to within ±3 volts of the target setting using a ten-turn potentiometer, and the flow rate was set to within ±1 mL/min of the target setting by controlling the speed of the gear pump. The test begins with a flow conditioning period lasting approximately 60 minutes, where the flow rate is set to 200 mL/min, and the voltage is set to 2 kV. Notice that the current and differential pressure readings reach steady state during this period. After the conditioning period, a

cycle of flow rates ranging from 0 to 300 mL/min is repeated for each voltage setting, which ranged from 500 to 3500 volts. Each flow rate setting is maintained for about five minutes to obtain steady state readings.

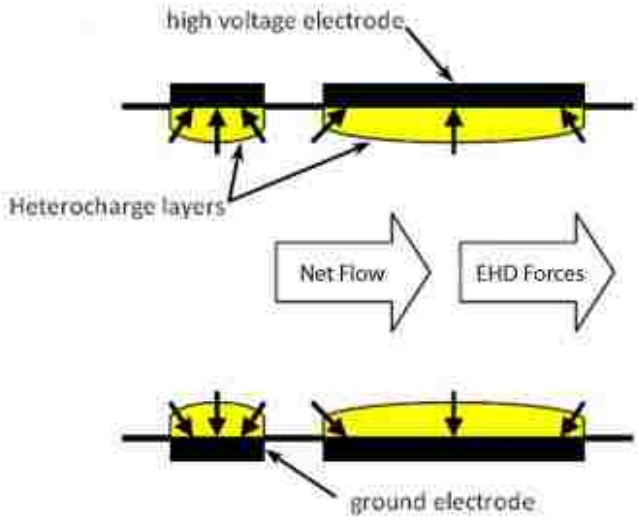

Figure 27: Forward flow tests: directions of pumping forces and net flow inside the EHD pump. Adapted from Pearson and Seyed-Yagoobi [25].

Figures 29, 30, and 31 below show the effects of flow velocity on the pressure reading, on the pressure generated by the EHD effects, and on the current consumption, respectively. Flow velocity is calculated as the average velocity through the EHD pump (volume flow rate divided by cross-section area). Each plot combines data from six tests performed on six different days. Data points from individual tests are the averages of 64 samples taken over two minutes from the center of each "step" in the flow rate cycle.

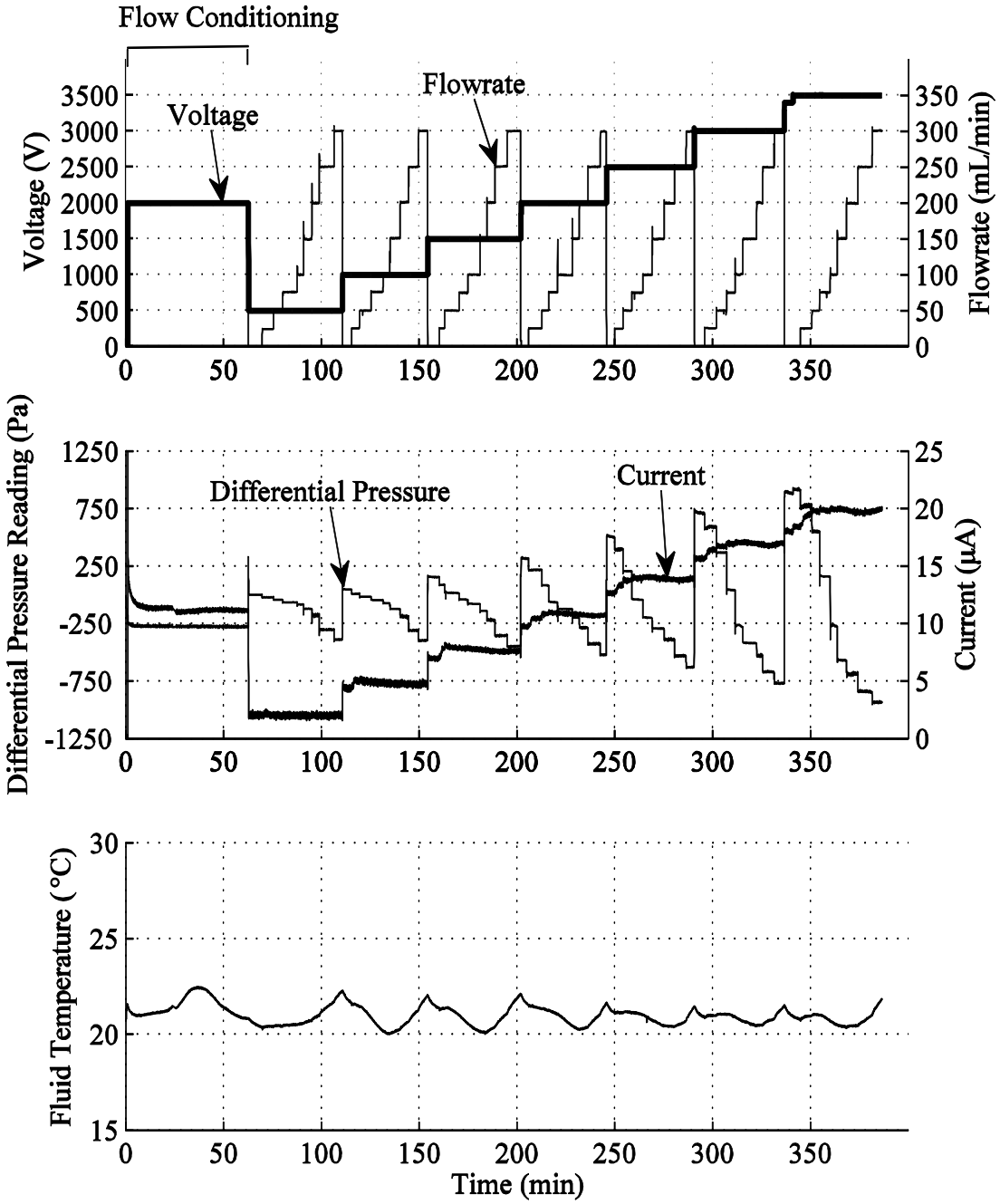

Figure 28: Sample forward flow test: inputs and results vs. time. Inputs are voltage and flow rate (top), results are differential pressure reading and current consumption (middle), and fluid temperature (bottom). Date: 2/21/2012.

Figure 29 shows the effect of flow velocity on differential pressure reading across the EHD pump at four different voltage settings. The flow velocity is expected to effect the differential pressure reading by two mechanisms: (1) increasing flow velocity will decrease the differential pressure reading because of friction, and (2) from equation (1.8) and from Yazdani and Seyed-Yagoobi [27], the flow velocity $\vec{u}$ changes the charge distribution near each electrode and decreases the thickness of the heterocharge layers, which decreases the Coulomb force and EHD pressure generation. The trend line for zero volts represents the pressure drop across the EHD pump due to friction only, and is the result of a curve-fit to data taken separately. Subtracting the contribution of friction from the differential pressure reading leaves only the contribution of EHD effects, which is shown in Figure 30.

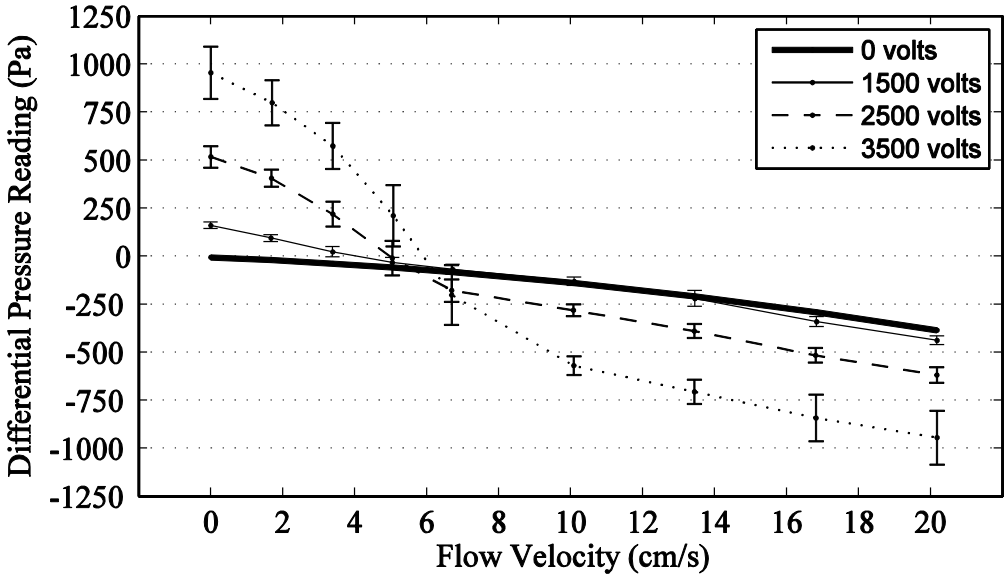

Figure 29: Forward flow tests: differential pressure reading vs. flow velocity for four voltage settings.

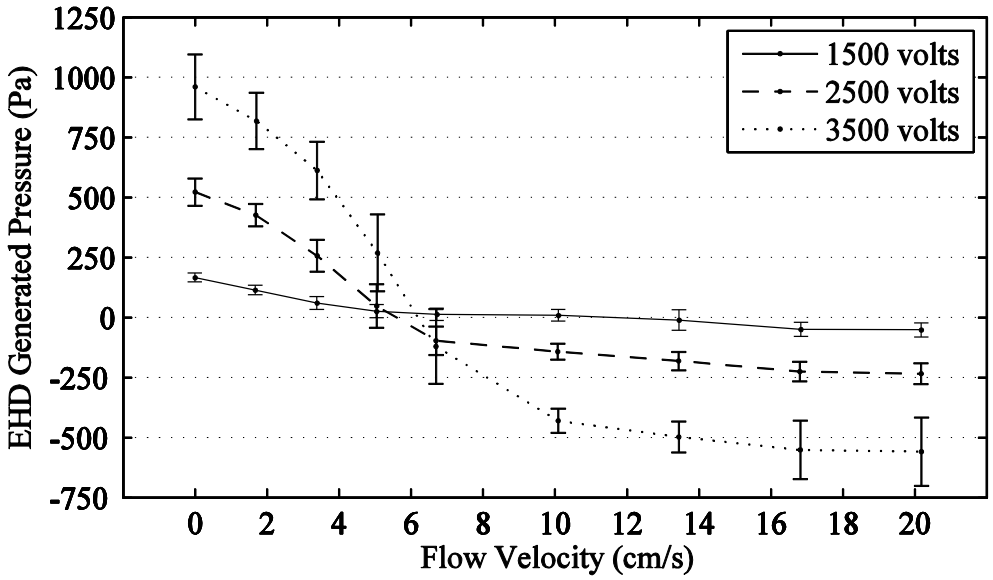

Figure 30: Forward flow tests: EHD generated pressure vs. flow velocity for three voltage settings.

In all six forward flow tests, the EHD generated pressure decreases with increasing flow velocity until reaching zero at a flow velocity around 6 cm/s. This behavior is consistent with the trend established by Feng and Seyed-Yagoobi [32], shown in Figure 10. This is the highest velocity at which the EHD pump can be expected to pump Novec 7600 and corresponds to a mass flow rate of approximately 133 grams per minute or 2.2 grams per second. Past this threshold, the EHD effects impose a pressure drop on the line, the magnitude of which depends mainly on the applied voltage. This behavior limits the capability of the EHD pump in the forward configuration to modify flow distribution in a flow network such as that found in the biologically-inspired TCS. The EHD pump will be able to increase the flow rate in its line only when the flow velocity is between 0 and 6 cm/s. Furthermore, the EHD pump will oppose any increases in flow rate which bring the velocity above 6 cm/s. This will be demonstrated in section

4.5. The mechanism which causes the pressure drop past the 6 cm/s threshold is unknown and may require simulation and direct visualization of the flow to completely understand. However, it is reasonable to say, based on Feng and Seyed-Yagoobi [32] and Yazdani and Seyed-Yagoobi [27], that a change in shape or a shift in the position of the heterocharge layer due to flow velocity is responsible. A shift or change in shape of the heterocharge layer would not be caused by transition from laminar to turbulent flow regimes because the maximum Reynolds number in the 1/4 inch tubing entering the pump is 1230, and through pump is 450.

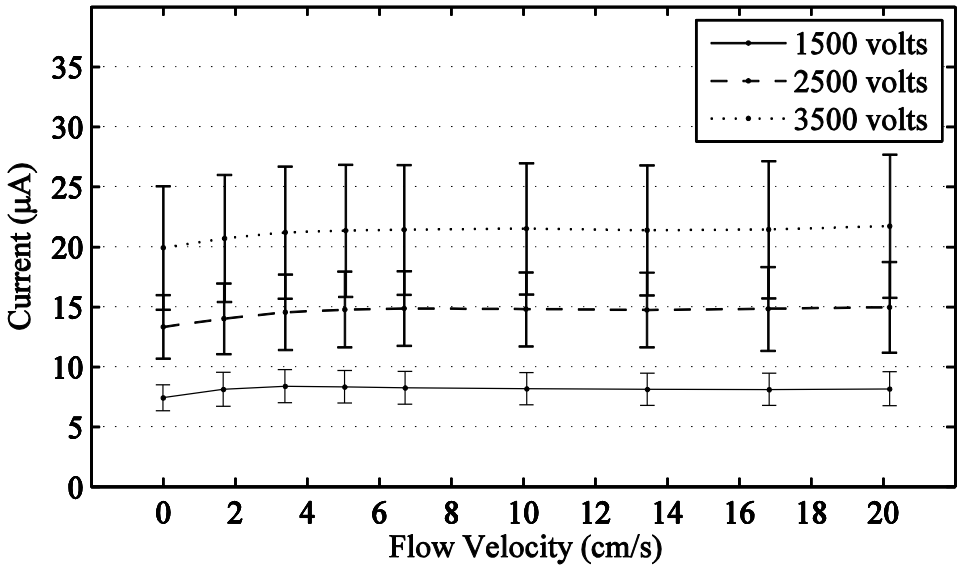

Figure 31: Forward flow tests: current vs. flow velocity for three voltage settings.

Figure 31 shows the effects of flow velocity on current for three voltage settings in forward flow tests. Because of large uncertainties caused by day-to-day variation in results, velocity does not appear to affect current consumption. According to the charge transport model discussed in section 1.3.2, increasing flow velocity should cause current

to rise slightly as the flow speeds up the motion of charges. As expected, the current consumption increases with applied voltage.

4.4. Reverse Flow Test Results

The procedure for reverse flow tests was identical to that of forward flow tests, except that the direction of pumping forces was reversed relative to the direction of flow velocity, as shown in Figure 32. Notice that the flow was in the same direction as in the forward flow tests (Figure 27), but the pump was oriented in the opposite direction. The test inputs of voltage and flow rate and the test results of differential pressure, current, and temperature are shown in Figure 33. Data shown in Figures 34, 35, and 36 are averages of data from seven tests performed on seven separate days, and uncertainty bars indicate the variation in readings across those seven tests. Figure 34 shows differential pressure readings across the EHD pump for four voltage settings. Because the EHD forces act in the upstream direction, and differential pressure is measured as downstream minus upstream pressure, the differential pressure reading is always negative.

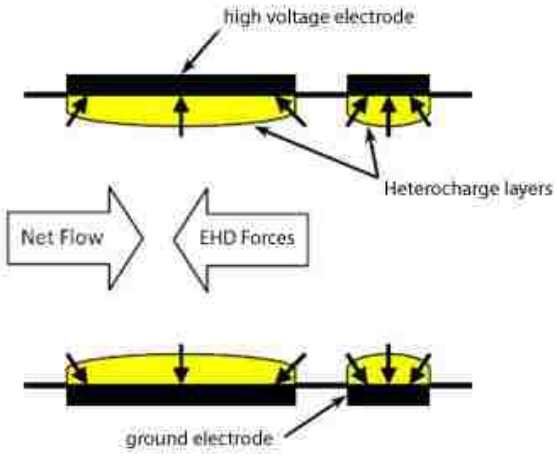

Figure 32: Reverse flow tests: directions of pumping forces and net flow inside the EHD pump. Adapted from Pearson and Seyed-Yagoobi [25].

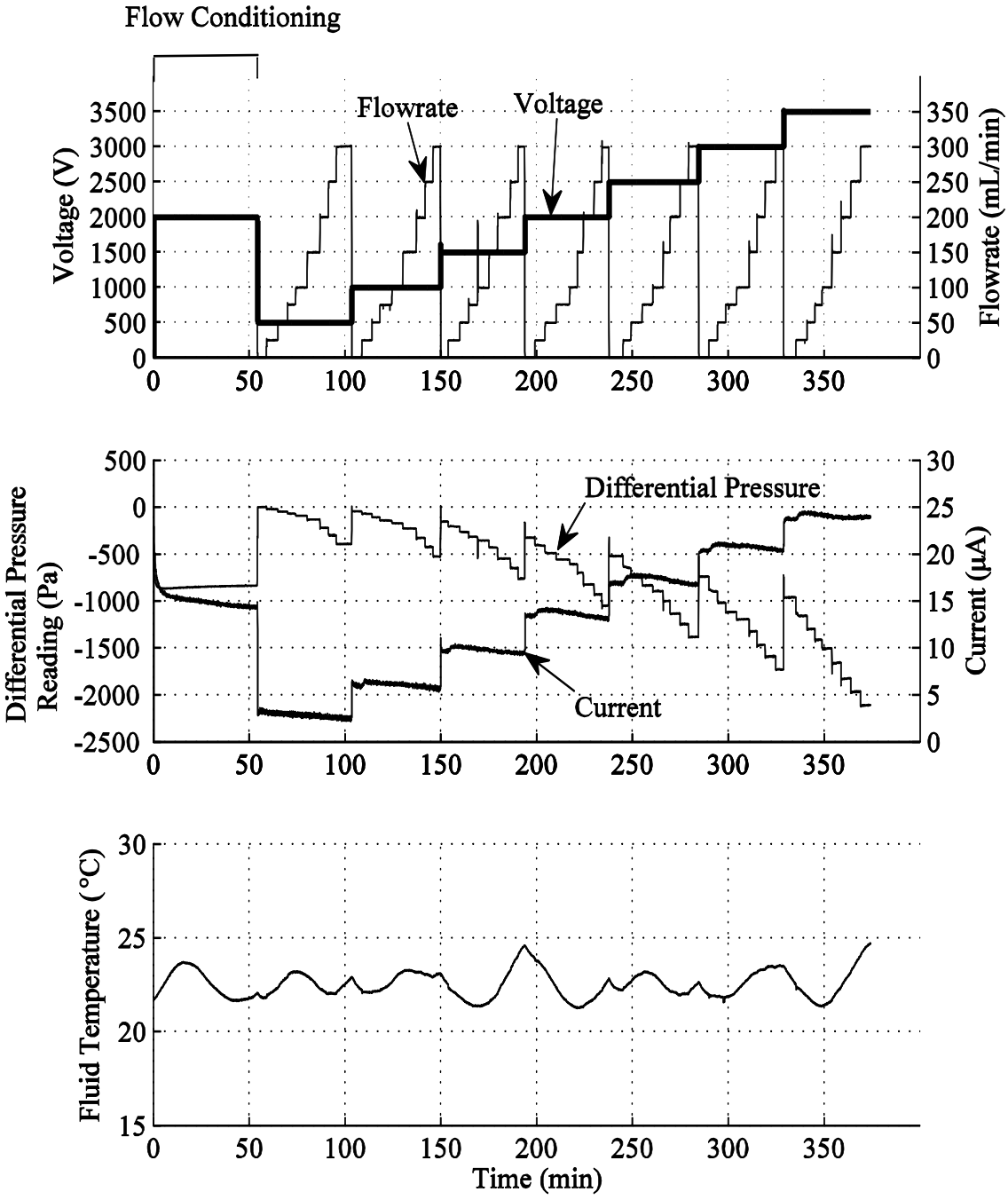

Figure 33: Sample reverse flow test: inputs and results vs. time. Inputs are voltage and flow rate (top), results are differential pressure reading and current consumption (middle), and fluid temperature (bottom). Date: 1/12/2012.

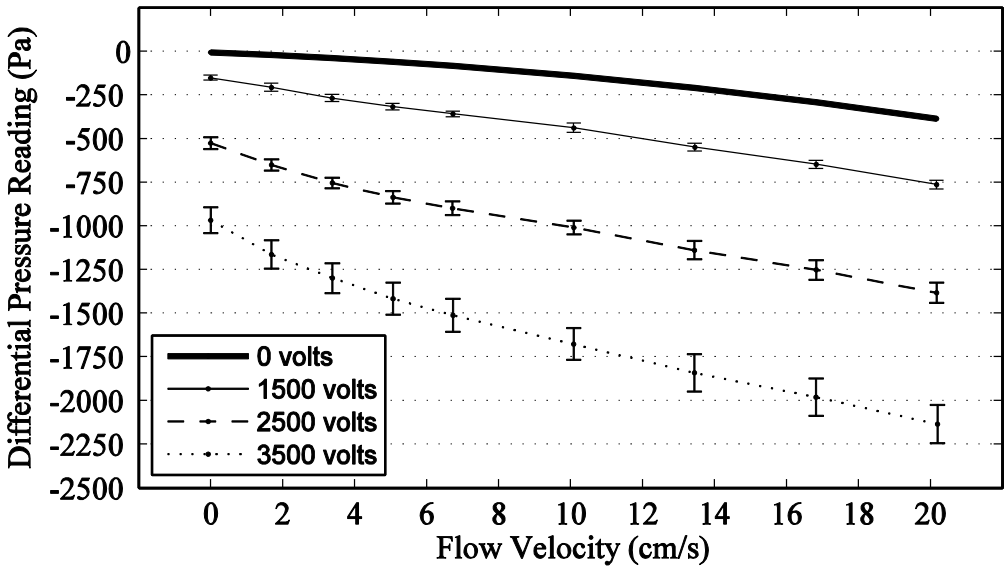

Figure 34: Reverse flow tests: differential pressure reading vs. flow velocity for four voltage settings.

The contribution of friction to the pressure reading is shown in Figure 34 as the line for zero volts. Once this contribution is subtracted from Figure 34, it is evident from Figure 35 that the negative pressure difference generated by EHD effects increases continually with flow velocity across the entire range of flow rates and increases with applied voltage at a given velocity. This a useful response, since the pressure drop created by EHD effects in the reverse configuration can be used to restrict flow in one line and reroute flow through a parallel line, as one would use a valve. This will be demonstrated in section 4.6.

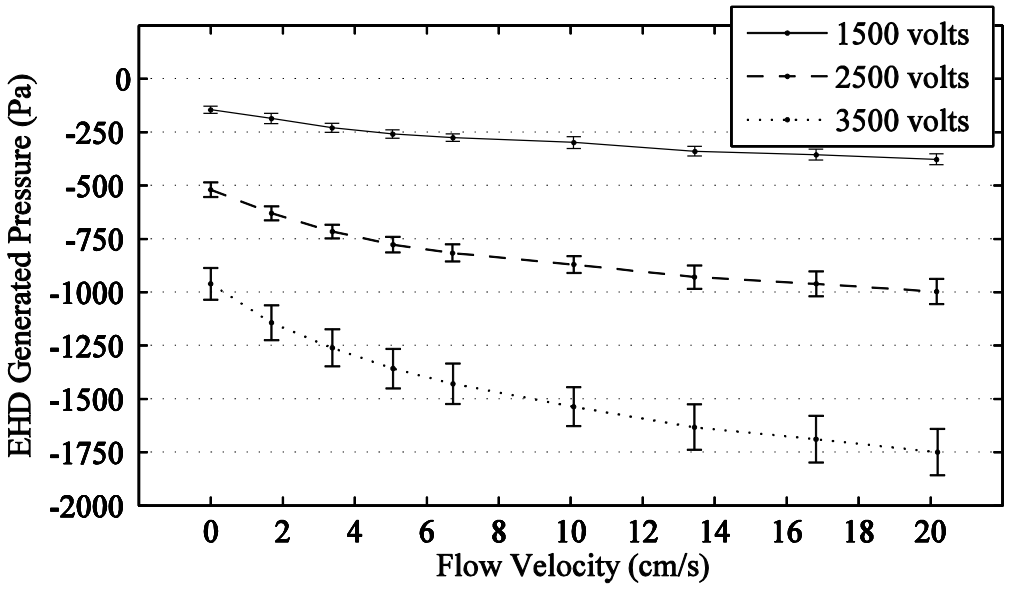

Figure 35: Reverse flow tests: EHD generated pressure vs. flow velocity for three voltage settings.

As in the forward flow tests, the current consumption shown in Figure 36 is not affected by increasing flow velocity. Given the variation in EHD generated pressure with flow velocity, the constant current consumption over the same range of velocities indicates that as the flow velocity increases, the efficiency with which the EHD pump resists flow increases. The average current readings for this type of test are several micro-amps higher than the average readings from the forward flow tests (Figure 31), while the static pressures (pressure at 0 cm/s) for the two tests are approximately equal. Therefore, the pump is consuming more power in these reverse flow tests than in the forward flow tests, for the same static pressure generation. This indicates a difference in the performance of the EHD pump, which may be caused by changing fluid properties.

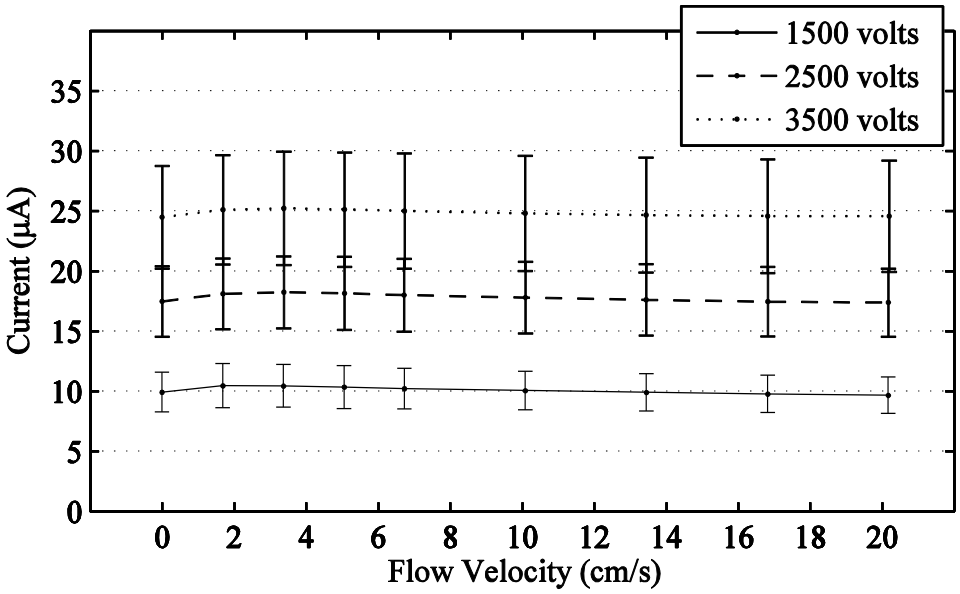

Figure 36: Reverse flow tests: current vs. flow velocity for three voltage settings.

4.5. Flow Distribution Configuration A Test Results

Flow distribution tests were used to determine which EHD pump configuration is more effective at modifying an existing distribution of flow through two parallel lines. Configuration A places the EHD pump in line (3) oriented so that the net pumping forces act in the same direction as the flow velocity (Figure 21). The input variables were varied in patterns similar to the forward and reverse flow tests, but as shown in Figure 37 (top), the voltage is repeatedly varied over a cycle for each total flow rate setting, not vice versa. The variables of pressure reading, current, and flow velocity in line (3) are also shown (middle and bottom). Increasing the total flow rate increases the flow rates in both lines (2) and (3). Consequently, the flow velocity in line (3) increases not only with the applied voltage but also with the total flow rate.

Figure 38 and Figure 39 show the EHD generated pressure and current results, respectively, versus the flow velocity in line (3) along with the corresponding results from the forward flow tests. Results from the two types of tests are consistent. Based on Figure 38 and Figure 39, the pump should be capable of increasing flow in line (3) only while flow velocities in that line are less than 6 cm/s. The flow rate results at the bottom of Figure 37 are consistent with this prediction. When the total flow rate is zero, EHD pump (a) drives flow around the small loop containing EHD pumps (a) and (b) (lines (2) and (3) in Figure 21). An increase in total flow rate increases the flow rate through both lines (2) and (3); EHD pump (a) is able to increase the flow through line (3) as applied voltages are increased. Notice that as the flow velocity in line (3) approaches 6 cm/s, increases in applied voltage have little effect on flow rate in that line.

Perhaps a more useful way of looking at the same phenomenon is to show the input power required by the EHD pump to change the flow distribution in line (3). Figure 40 shows the flow pump power input versus flow velocity in line (3) for three settings of total flow rate. The seven power levels in the figure correspond to the seven voltage settings between 500 and 3500 volts. These data are averages over four tests performed on four different days. Again, as flow velocity approaches 6 cm/s, additional power does little to affect the distribution of flow between lines (2) and (3). Uncertainty bars on these data are very large because some tests were performed months apart, and it is likely that fluid properties changed over that period. Mass flow rates are based on a density of 1545 kg/m^3 at 22 °C. Table 8 gives the maximum input power consumed at 3500 volts and the resulting changes in velocity and mass flow rate in line (3) for three settings of total flow rate.

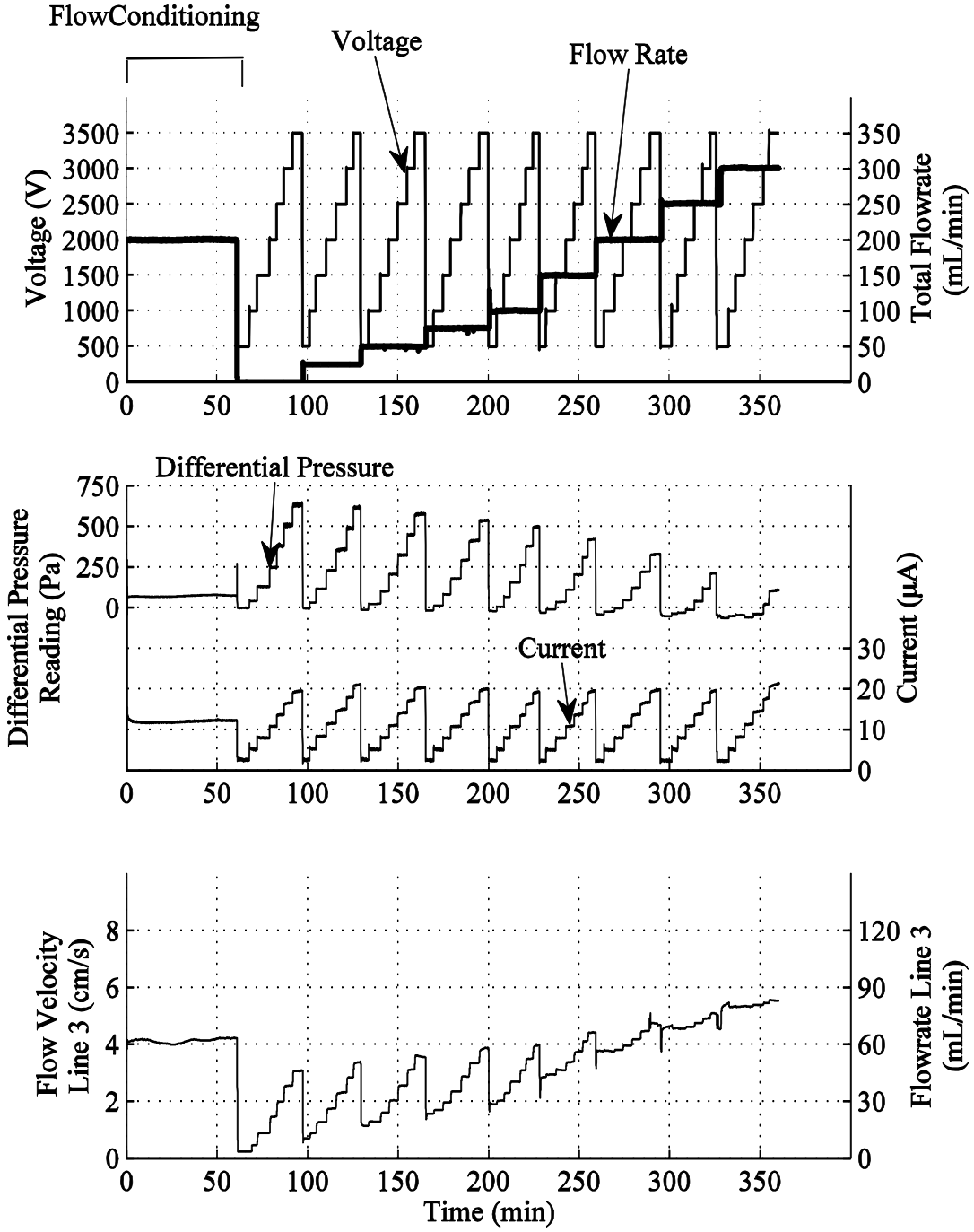

Figure 37: Sample distribution test configuration A: inputs and results vs. time. Inputs are voltage and flow rate (top), results are EHD generated pressure and current consumption (middle), and flow velocity in line (3) (bottom). Date: 2/28/2012.

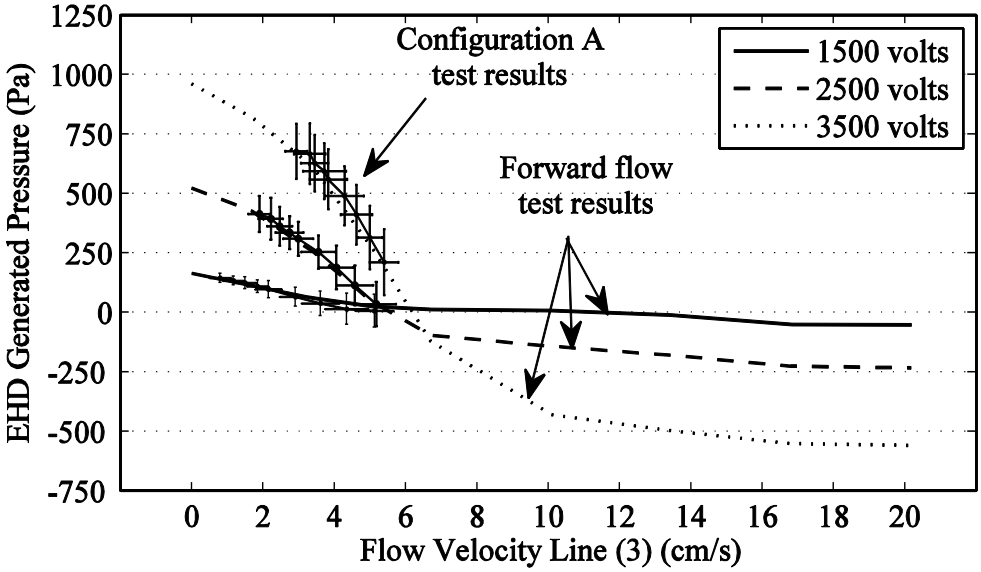

Figure 38: Pressure generation data from forward flow tests and from the configuration A distribution tests vs. flow velocity in line (3).

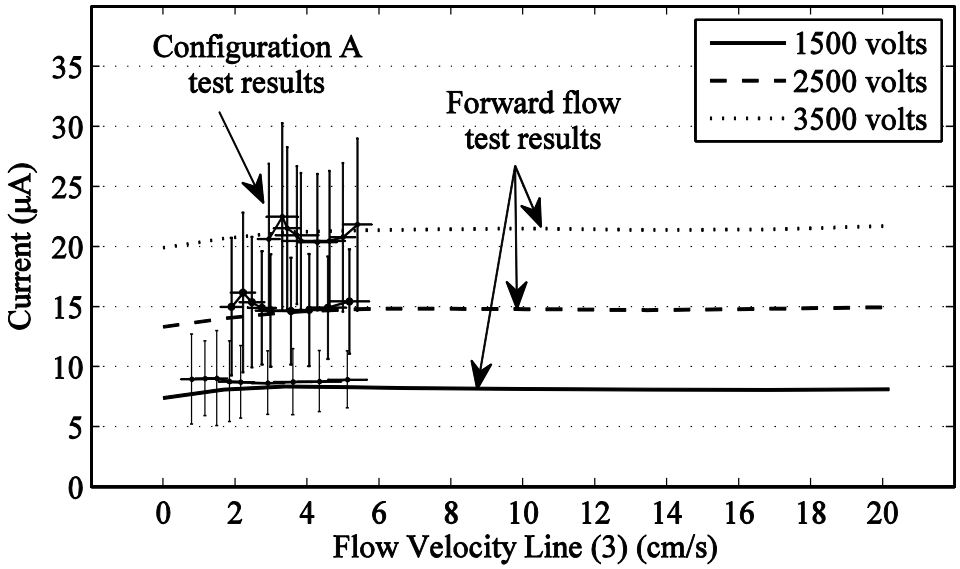

Figure 39: Current data from forward flow tests and from the configuration A distribution tests vs. flow velocity in line (3).

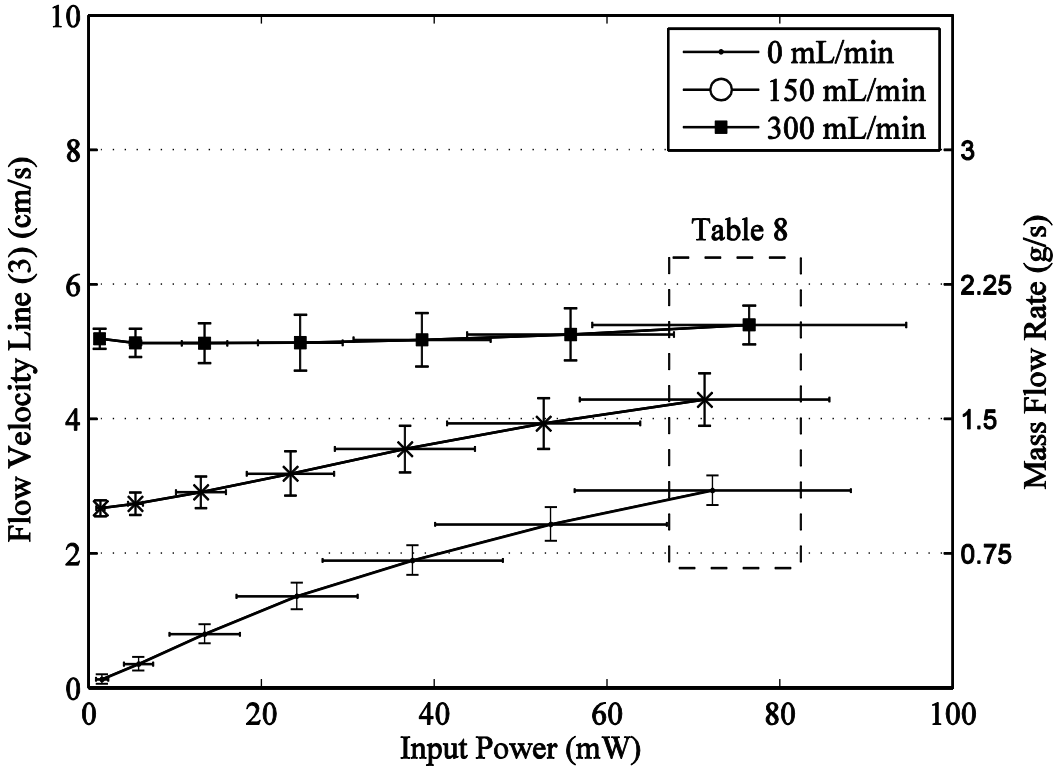

Figure 40: Flow distribution tests configuration A: flow velocity in line (3) vs. pump input power for three settings of total flow rate.

Table 8: Configuration A: Maximum input power (at 3500 volts) and the resulting increases in velocity and mass flow rate in line (3) for three settings of total flow rate shown in Figure 40.

Total Flow Rate (mL/min)	Input Power (mW)	Δ Velocity Line (3) (cm/s)	Δ Mass Flow Rate Line (3) (g/s)	% Change in Velocity Line (3)
0	72	2.9	1.1	
150	71	1.6	0.6	60
300	76	0.2	0.07	4

The results of the forward flow tests also predict that power input to the EHD pump while the internal flow velocity exceeds 6 cm/s results in a reduction of the flow rate in line (3) due to a pressure drop induced by EHD effects. Flow velocities in line (3)

did not exceed the 6 cm/s threshold in these four tests because the pressure drop across the flow meter in line (3) was too high. Therefore, the results of two more tests are shown in Figure 41, where a valve was used to modify the pressure drop in lines (2) and (3). These results illustrate the effects of the EHD pump on flow distribution for velocities exceeding 6 cm/s in line (3). These two tests were performed after low fluid levels required that the system be emptied and refilled with fresh fluid. Thus these results cannot be compared directly to the previous four tests because the fluid properties are probably different. However, the trends in these data are consistent with predictions of the forward flow tests. At a total flow rate of 250 mL/min, the velocity in line (3) is 9.4 cm/s at 0.7 mW of input power (lowest power setting). When the input power is increased to 35 mW (highest power setting), the velocity in line (3) drops to 9 cm/s.

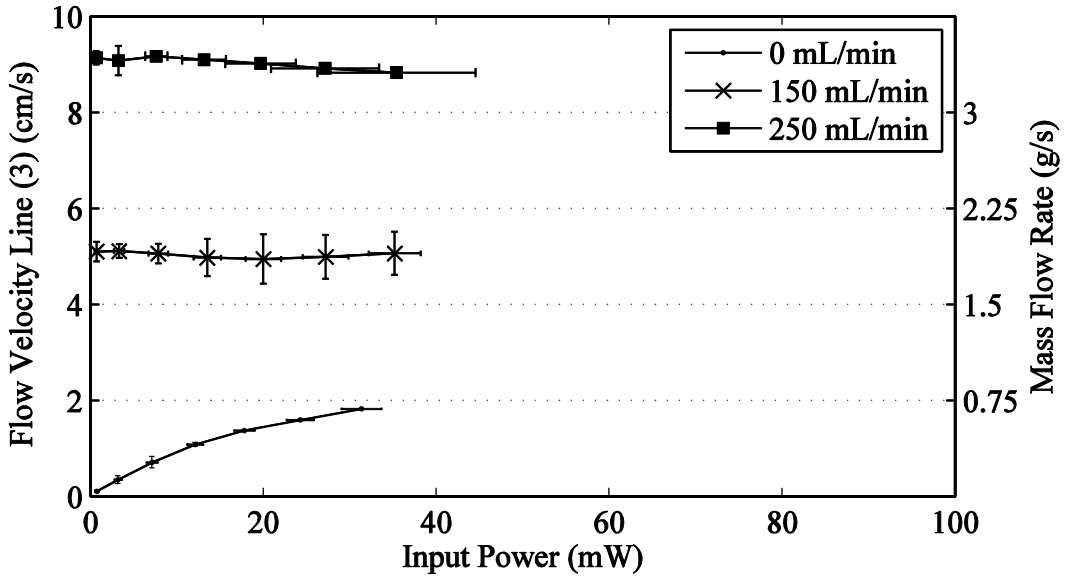

Figure 41: Flow distribution tests configuration A using new fluid: flow velocity in line (3) vs. pump input power for three settings of total flow rate.

4.6. Flow Distribution Configuration B Test Results

Configuration B places EHD pump (a) in line (2) oriented so that the net pumping forces act in the direction opposite to the flow velocity (Figure 21). The applied voltage and total flow rate inputs follow the same patterns as for configuration A. Figure 42 shows the voltage and flow rate settings (top), the differential pressure and current readings (middle), and the resulting flow velocities in line (3) (bottom). Increasing the total flow rate increases the flow rates in both lines (2) and (3). Consequently, the flow velocity in line (3) increases not only with the applied voltage but also with the total flow rate.

Figure 43 and Figure 44 give the EHD generated pressure and current results, respectively, versus flow velocity in line (2) along with the corresponding results from the reverse flow tests. Pressure data between the configuration B tests and reverse flow tests agree; note that increases in the flow velocity in line (2) do not suppress the pump's ability to generate pressure as in the forward flow and configuration A tests. Current consumption during the configuration B tests is lower than expected and is closer in magnitude to the results from the forward flow and configuration A distribution tests. Therefore, current readings from all but the reverse flow tests are similar. Negative velocities in these two figures are the result of flow driven by the EHD pump around the small loop containing EHD pumps (a) and (b) (lines (2) and (3) in Figure 21).

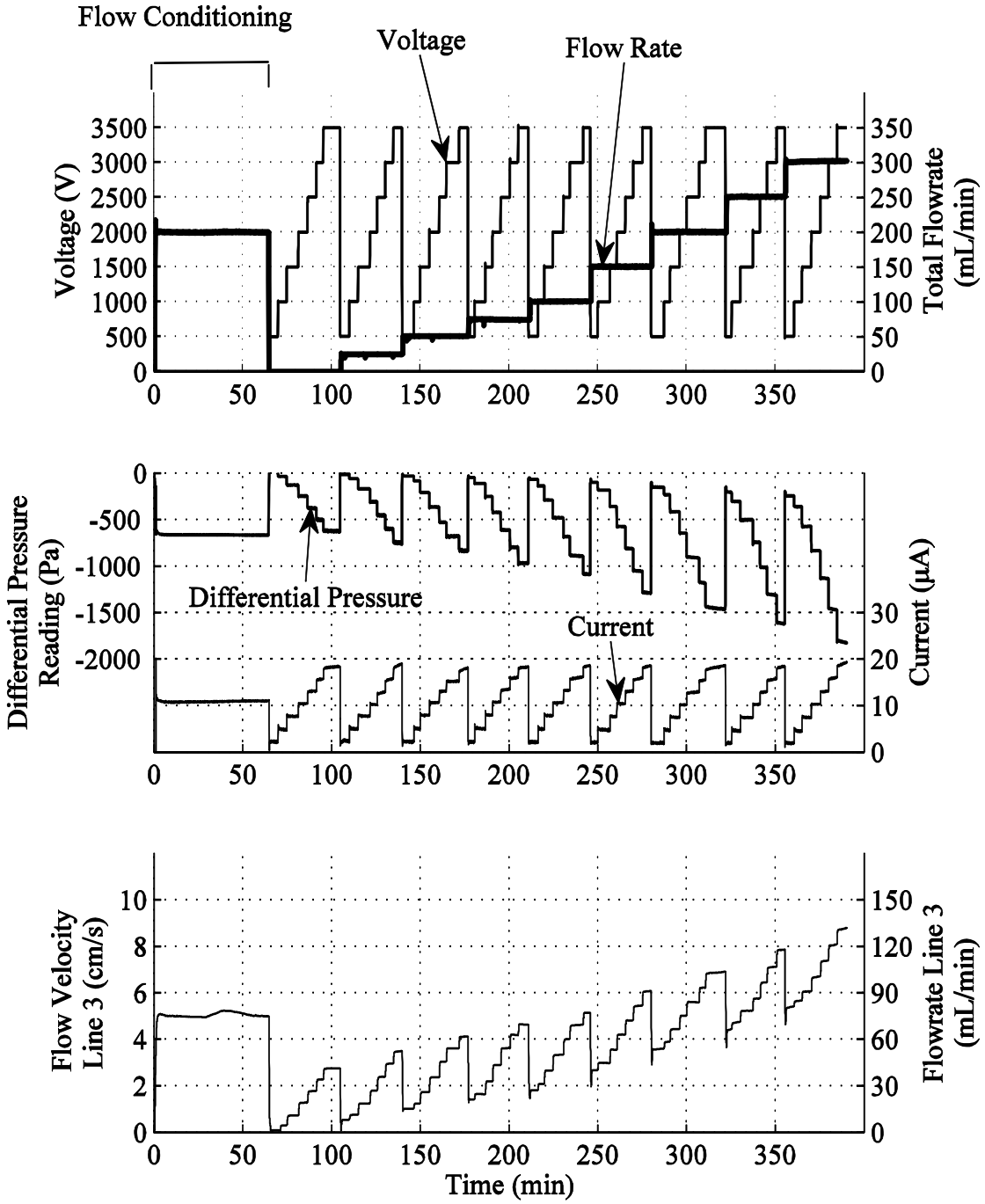

Figure 42: Sample distribution test Case B: inputs and results vs. time. Inputs are voltage and flow rate (top), results are EHD generated pressure and current consumption (middle), and flow velocity in line (3) (bottom). Date: 2/15/2012.

Based on Figure 43 and Figure 44, an increase in power applied to the EHD pump increases the pressure drop in line (2) and should thereby decrease flow velocity in line (2) and increase flow velocity in line (3). Figure 45 shows the velocity in line (3) versus the power required by the EHD pump. The seven power levels in the figure correspond to the seven voltage settings between 500 and 3500 volts. These results are averages over six separate tests, performed on six different days. When the total flow rate is zero, EHD pump (a) drives flow around the small loop containing EHD pumps (a) and (b) (lines (2) and (3) in Figure 21). An increase in total flow rate increases the flow rate through both lines (2) and (3); EHD pump (a) is able to increase the flow through line (3) as applied voltages are increased. Because increases in flow velocity in line (2) do not suppress the pump's ability to generate pressure, the pump's ability to modify the flow distribution is not diminished, as was the case in configuration A tests. For instance, at a total flow rate of 300 mL/min, application of 76 mW to the EHD pump in the configuration A tests increases the velocity in line (3) by 0.21 cm/s, or 4% (Figure 40), while application of 72 mW to the EHD pump in configuration B tests increases the velocity in line (3) by 3.6 cm/s, or 66% (Figure 45). Values of maximum power input (at 3500 volts), change in velocity, and change in mass flow rate in line (3) for configuration B are listed in Table 9 below. Comparison of Table 8 to Table 9 clearly suggests that for the purposes of controlling flow distribution, EHD pumps are more effectively employed as valves, as in configuration B in Figure 12, than as pumps, as in configuration A in Figure 12.

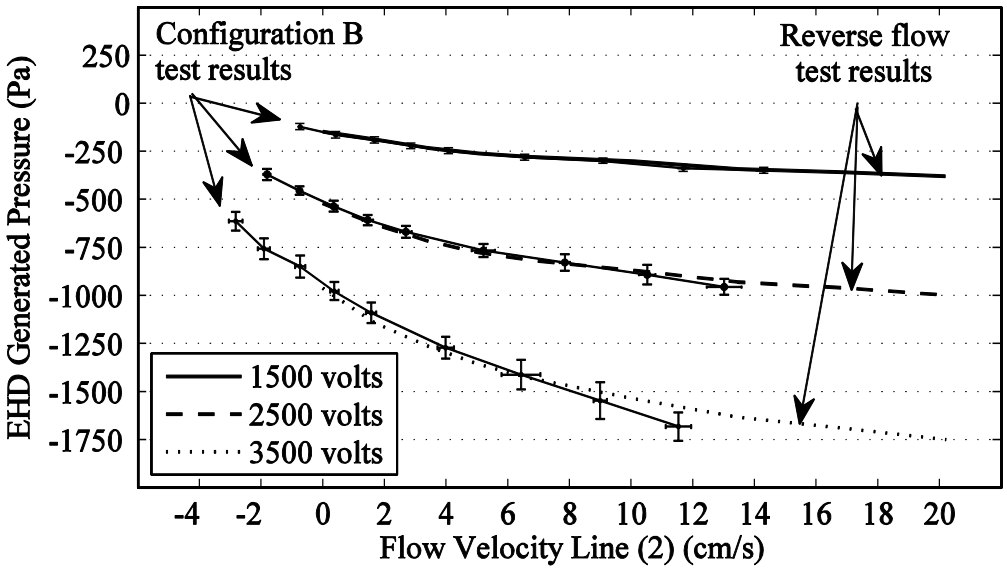

Figure 43: Pressure generation data from reverse flow tests and from the configuration B distribution tests vs. flow velocity in line (2).

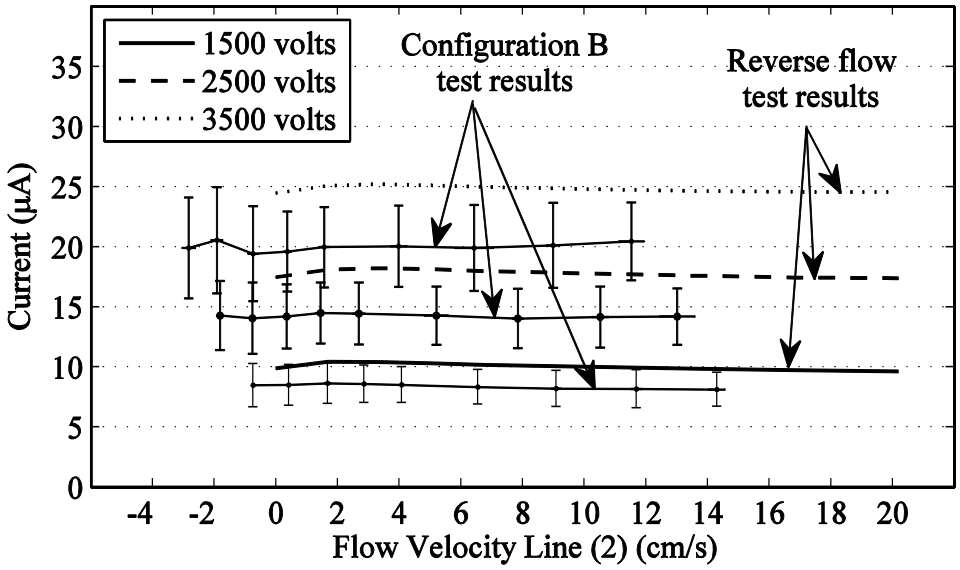

Figure 44: Current data from reverse flow tests and from the configuration B distribution tests vs. flow velocity in line (2).

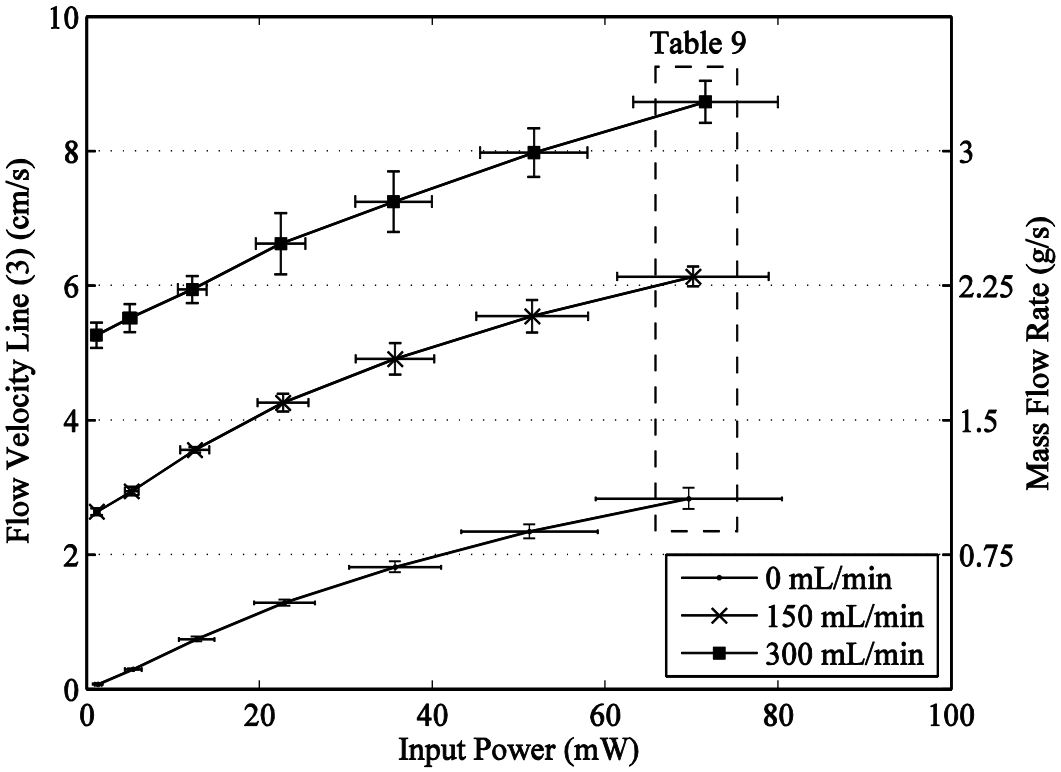

Figure 45: Flow distribution tests configuration B: flow velocity in line (2) vs. pump input power for four settings of total flow rate.

Table 9: Configuration B: Maximum input power (at 3500 volts) and the resulting increases in velocity and mass flow rate in line (3) for three settings of total flow rate shown in Figure 45.

Total Flow Rate (mL/min)	Input Power (mW)	Δ Velocity Line (3) (cm/s)	Δ Mass Flow Rate Line (3) (g/s)	% Change in Velocity Line (3)
0	70	2.8	1.1	
150	70	3.5	1.3	132
300	72	3.5	1.3	66

5. Conclusions and Future Work

This project was intended as a first step in understanding the performance characteristics of flush electrode EHD pumps under various flow conditions and their capabilities to control the distribution of flow in two parallel lines when in configurations A and B shown in Figure 12. Results will help guide future efforts at using EHD pumps to control flow distribution in the biologically-inspired TCS and may lead to further studies on the EHD conduction phenomenon around flush electrode designs.

The work partially accomplished the two experimental objectives listed in section 2.2. Though one can make qualitative statements regarding the performance of the EHD pump under various flow conditions and its capabilities of redistributing flow in the two configurations, the causes of day-to-day variation in performance remain unknown. Therefore, the levels of pressure generation and power consumption observed cannot be used with confidence.

The response of the fluid to the sudden application of an electric field in static tests is similar qualitatively to results by Pearson and Seyed-Yagoobi [25], and shows that the EHD conduction phenomenon is the dominant source of pressure generation, rather than ion-injection, which would produce a pressure gradient in the opposite direction to what was observed. Performance characteristics of the two constructed EHD pumps were not the same despite identical fabrication and assembly procedures. Further, benchmark tests using pump (a) only were not repeatable over several months of testing. The latter problem emphasizes the importance of maintaining the purity of the working fluid, or monitoring the electrical properties of the fluid so that testing can be conducted with the fluid at a known state. The voltage-pressure and voltage-current characteristics

show that both pressure difference and current consumption increase with the strength of the applied electric field. The observed linear voltage-current characteristic is consistent with an increase in velocity of charges due to increasing Coulomb force, as discussed in section 1.3.2.

When the EHD pump is oriented so that net pumping forces are aligned with the velocity of an oncoming flow, the effects of increasing flow velocity are to first decrease the EHD pressure generation, then past a velocity threshold of about 6 cm/s, to reverse the direction of the net EHD pumping forces. This limits the capability of the EHD pump in configuration A to affect the distribution of flow in parallel lines. It was demonstrated in flow distribution tests that while velocities are below the threshold, increasing input power increased flow velocity through the pump but that increasing flow velocity suppressed the pump's ability to further increase flow. It was also demonstrated that while flow velocities are above the threshold, increasing the power applied to the pump will decrease the flow rate in the line. However, in this regime, there is no penalty to pressure generation for increasing flow velocities further. This phenomenon may be caused by a change in the shape of the heterocharge layers surrounding the electrodes. Modeling and simulation and perhaps direct flow visualization will be required to establish the cause. Furthermore, testing using other fluids, and using pumps with different electrode thicknesses, flow cross-sections, or fabrication methods, will need to reproduce these results to rule out the possibility that the response is somehow unique to this pump design.

When the EHD pump is oriented so that net pumping forces act in the direction opposite to an oncoming flow, increasing flow velocity enhances pressure generation

rather than suppressing it as in configuration A distribution tests. For all flow velocities in configuration B, increasing input power significantly increased flow rate in line (3) by decreasing flow in line (2). Comparison of results from the two flow distribution tests leads to the conclusion that configuration B is more effective than configuration A for increasing flow in line (3). One may extend this conclusion to the biologically-inspired TCS in Figure 12 to argue that configuration B, which uses EHD pumps as valves, will be more effective than configuration A in re-routing flow through face-sheet channels.

In both forward and reverse flow tests, current consumption was dependent mainly on the strength of the electric field and was not affected by changing flow velocity, indicating that the primary means of charge transport is charge migration due to the Coulomb force. Current consumption in the reverse flow tests was several μA higher than in the other three flow tests, possibly due to a difference in fluid properties.

Detailed analysis of the EHD-generated flows close to the channel walls will likely give heat transfer coefficients different from those of pressure-driven internal flow because the normal boundary layers and flow development patterns are disrupted by the EHD pumping forces. The numerical investigation of Yazdani and Seyed-Yagoobi [40] predicts multiple vortices near the liquid-electrode interface and considerable improvement of the heat transfer coefficient compared to that of the pressure-driven case. Future studies to determine flow paths through the biologically-inspired TCS, flow rates, and pump locations should include characterization of this enhanced heat transfer capability.

Further work is also needed to characterize the flow conditioning process mentioned in sections 3.3 and 4.1. It is clear from Figure 24 that a conditioning process can change the equilibrium levels of current consumption and pressure generation, but the underlying mechanics of the process have not been investigated. Before EHD pumps can be employed in a thermal control system, this process must be fully understood.

References

[1] Williams, A. D. and Palo, S. E. "Issues and Implications of the Thermal Control System on the “Six Day Spacecraft”." Paper No. RS4-2006-6001. *4th Responsive Space Conference 2006*, Los Angeles, CA, April 24–27, 2006.

[2] "Plan for Operationally Responsive Space; A Report to Congressional Defense Committees." Department of Defense. April 17, 2007. URL: http://www.responsivespace.com/Conferences/RS5/4=17=07%20ORS%20Plan.pdf [cited: June 5, 2011].

[3] Arritt, B. J., Buckley, S. J., Ganley, J. M., Welsh, J. S., Henderson, B. K., Lyall, M. E., Williams, A. D., Prebble, J. C., DiPalma, J., Mimovich, M. and Roopnarine, R. "Development of a Satellite Structural Architecture for Operationally Responsive Space." AIAA Paper 2008-1772. *49th AIAA/ASME/ASCE/AHS/ASC Structures, Structural Dynamics, and Materials Conference*, Schaumburg, IL, April 7-8, 2008.

[4] Williams, A. D., Lyall, M. E., Hengeveld, D. W. and Young, Q. E. "Thermal Control System Requirements and Challenges for a Responsive Satellite Bus." *Proceedings of SPIE*, *Sensors and Systems for Space Applications III*, Vol. 7330, pp. 73300E.

[5] Hengeveld, D. W., Braun, J. E., Groll, E. A. and Williams, A. D. "Determination of Hot- and Cold-Case Design Orbits for Robust Thermal Control Subsystem Design." AIAA Paper 2008-1956. *49th AIAA/ASME/ASCE/AHS/ASC Structures, Structural Dynamics, and Materials Conference*, Schaumburg, IL, April 7-10, 2008.

[6] Hengeveld, D. W., Braun, J. E., Groll, E. A. and Williams, A. D. "Optimal Component Placement to Minimize Thermal Management Requirements by Approaching a Uniform Distribution of Applied Fluxes." AIAA Paper 2009-2223. *50th AIAA/ASME/ASCE/AHS/ASC Structures, Structural Dynamics, and Materials Conference*, Palm Springs, CA, May 4-7, 2009.

[7] Williams, A. D., Arritt, B. J., Diaz-Aguado, M., Taft, B. and Nieuwkoop, A. "Biologically Inspired Thermal-Structural Satellite Panels." AIAA Paper 2007-2183. *48th AIAA/ASME/ASCE/AHS/ASC Structures, Structural Dynamics, and Materials Conference*, Honolulu, HI, April 23-26, 2007.

[8] Williams, A. D., Lyall, M. E., Underwood, L. E., Arritt, B. J. and Taft, B. "Biologically Inspired Multifunctional Composite Panel with Integrated Circulatory System for Thermal Control." *Proceedings of the 17th International Conference on Composite Materials ICCM-17*, Edinburgh, UK, July 27 - 31, 2009.

[9] Melcher, J. R. *Continuum Electromechanics*. The MIT Press, Cambridge, MA, 1981.

[10] Stuetzer, O. M. "Ion Drag Pressure Generation." *Journal of Applied Physics*, Vol. 30, No. 7, 1959, pp. 978-981.

[11] Pickard, W. F. "Ion Drag Pumping. I. Theory." *Journal of Applied Physics*, Vol. 34, No. 2, 1963, pp. 246-250.

[12] Pickard, W. F. "Ion Drag Pumping. II. Experiment." *Journal of Applied Physics*, Vol. 34, No. 2, 1963, pp. 251-258.

[13] Melcher, J. R. "Traveling-wave Induced Electro-convection." *Physics of Fluids*, Vol. 9, No. 8, 1966, pp. 1548-1555.

[14] Brand, K. and Seyed-Yagoobi, J. "Experimental Study of Electrohydrodynamic Induction Pumping of a Dielectric Micro Liquid Film in External Horizontal Condensation Process." *Journal of Heat Transfer*, Vol. 125, No. 6, 2003, pp. 1096-1105.

[15] Seyed-Yagoobi, J. "Electrohydrodynamic Pumping of Dielectric Liquids." *Journal of Electrostatics*, Vol. 63, No. 6-10, 2005, pp. 861-869.

[16] Gallagher, T. J. *Simple Dielectric Liquid—Mobility, Conduction, and Breakdown*. Clarendon, Oxford, UK, 1975.

[17] Adamczewski, I. *Ionization, Conductivity and Breakdown in Dielectric Liquids*. Barnes & Noble, New York, NY, 1969.

[18] Felici, N. J. "D.C. Conduction in Liquid Dielectrics (Part 2)." *Direct Current*, Vol. 2, 1971a, pp. 147-165.

[19] Felici, N. J. "D.C. Conduction in Liquid Dielectrics (Part 1)." *Direct Current*, Vol. 2, 1971b, pp. 90-99.

[20] Castellanos, A. "Conduction and Polarization." *Electrohydrodynamics,* Ed. A. Castellanos. Springer, New York, NY, 1998, pp. 20-40.

[21] Onsager, L. "Deviations from Ohm's Law in Weak Electrolytes." *Journal of Chemical Physics*, Vol. 2, No. 9, 1934, pp. 599-614.

[22] Wikipedia, "Double layer (interfacial)," URL: http://en.wikipedia.org/wiki/Double_layer_(interfacial) [cited September 11, 2011].

[23] Felici, N. J. "A Tentative Explanation of the Voltage-current Characteristic of Dielectric Liquids." *Journal of Electrostatics*, Vol. 12, No. 1, 1982, pp. 165-172.

[24] Alj, A., Denat, A., Gosee, J. P. and Gosse, B. "Creation of Charge Carriers in Nonpolar Liquids." *IEEE Transactions on Electrical Insulation*, Vol. EI-20, No. 2, 1985, pp. 221-231.

[25] Pearson, M. R. and Seyed-Yagoobi, J. "Experimental Study of EHD Conduction Pumping at the Meso- and Micro-Scale." *Journal of Electrostatics*, Vol. 69, No. 6, 2011, pp. 479-485.

[26] Pearson, M. R. and Seyed-Yagoobi, J. "Advances in Electrohydrodynamic Conduction Pumping." *IEEE Transactions on Dielectrics and Electrical Insulation,* Vol. 16, No. 2, 2009, pp. 424-434.

[27] Yazdani, M. and Seyed-Yagoobi, J. "Electrically Induced Dielectric Liquid Film Flow Based on Electric Conduction Phenomenon." *IEEE Transactions on Dielectrics and Electrical Insulation*, Vol. 16, No. 3, 2009, pp. 768-777.

[28] Lyall, M. E., Williams, A. D., Arritt, B. J. and Taft, B. S. "Experimental Analysis of a Biologically Inspired Thermal-Structural Satellite Panel." AIAA Paper 2008-1833. *49th AIAA/ASME/ASCE/AHS/ASC Structures, Structural Dynamics, and Materials Conference*, Schaumburg, IL, April 7-10, 2008.

[29] Jeong, S.-I. and Didion, J. "Thermal Control Utilizing an Electrohydrodynamic Conduction Pump in a Two-Phase Loop With High Heat Flux Source." *ASME Journal of Heat Transfer*, Vol. 129, No. 11, 2007, pp. 1576-1583.

[30] Jeong, S.-I. and Didion, J. "Performance Characteristics of Electrohydrodynamic Conduction Pump in Two-Phase Loops." *Journal of Thermophysics and Heat Transfer*, Vol. 22, No. 1, 2008, pp. 90-97.

[31] Feng, Y. and Seyed-Yagoobi, J. "Control of Liquid Flow Distribution Utilizing EHD Conduction Pumping Mechanism." *IEEE Transactions on Industry Applications*, Vol. 42, No. 2, 2006, pp. 369-377.

[32] Feng, Y. and Seyed-Yagoobi, J. "Electrical Charge Transport and Energy Conversion with Fluid Flow during Electrohydrodynamic Conduction Pumping." *Physics of Fluids*, Vol. 19, No. 5, 2007, pp. 057102.

[33] Crowley, J. M., White, G. S. and Chato, J. C. "Selecting a Working Fluid to Increase the Efficiency and Flow Rate of an EHD Pump." *IEEE Transactions on Industry Applications*, Vol. 26, No. 1, 1990, pp. 42-49.

[34] Incropera, F. P., Dewitt, D. P., Bergman, T. L. and Lavine, A. S. *Fundamentals of Heat and Mass Transfer, Sixth Edition*. Wiley, 2007, p. 519.

[35] Donaldson, S. A. and Miracle, D. B. *ASM Handbook Volume 21: Composites, Tenth Edition*. ASM International, 2001, p. 1096.

[36] Wertz, J. R. and Larson, W. J. *Space Mission Analysis and Design*. Kluwer Academic Publishers, Boston, MA, 1999, p. 428.

[37] Abernathy, R. B., Benedict, R. P. and Dowdell, R. B. "ASME Measurement Uncertainty." *ASME Journal of Fluids Engineering*, Vol. 107, No. 2, 1985, pp. 161-164.

[38] Coleman, H. W. and Steele, W. G. *Experimentation and Uncertainty Analysis for Engineers*. Wiley, New York, NY, 1989, p. 273.

[39] Kline, S. J. and McClintock, F. A. "Describing Uncertainties in Single Sample Experiments." *Mechanical Engineering*, Vol. 75, No. 1, 1956, pp. 3-8.

[40] Yazdani, M. and Seyed-Yagoobi, J. "Numerical Investigation of Electrohydrodynamic-Conduction Pumping of Liquid Film in the Presence of Evaporation." *ASME Journal of Heat Transfer*, Vol. 131, No. 1, 2009, pp. 011602.